

## Toward ice formation closure in Arctic mixed-phase boundary layer clouds during ISDAC

Alexander Avramov,<sup>1,2</sup> Andrew S. Ackerman,<sup>3</sup> Ann M. Fridlind,<sup>3</sup> Bastiaan van Dierenhoven,<sup>1</sup> Giovanni Botta,<sup>4,5</sup> Kultegin Aydin,<sup>5</sup> Johannes Verlinde,<sup>4</sup> Alexei V. Korolev,<sup>6</sup> J. Walter Strapp,<sup>6</sup> Greg M. McFarquhar,<sup>7</sup> Robert Jackson,<sup>7</sup> Sarah D. Brooks,<sup>8</sup> Andrew Glen,<sup>8</sup> and Mengistu Wolde<sup>9</sup>

Received 4 March 2011; revised 7 July 2011; accepted 15 July 2011; published 13 October 2011.

[1] A modeling study of a low-lying mixed-phase cloud layer observed on 8 April 2008 during the Indirect and Semi-Direct Aerosol Campaign is presented. Large-eddy simulations with size-resolved microphysics were used to test the hypothesis that heterogeneous ice nucleus (IN) concentrations measured above cloud top can account for observed ice concentrations, while also matching ice size distributions, radar reflectivities, and mean Doppler velocities. The conditions for the case are favorable for the hypothesis: springtime IN concentrations are high in the Arctic, the predominant ice habit falls slowly, and overlying IN concentrations were greater than ice particle number concentrations. Based on particle imagery, we considered two dendrite types, broad armed (high density) and stellar (low density), in addition to high and low density aggregates. Two simulations with low-density aggregates reproduced observations best overall: one in which IN concentrations aloft were increased fourfold (as could have been present above water saturation) and another in which initial IN concentrations were vertically uniform. A key aspect of the latter was an IN reservoir under the well-mixed cloud layer: as the simulations progressed, the reservoir IN slowly mixed upward, helping to maintain ice concentrations close to those observed. Given the uncertainties of the measurements and parameterizations of the microphysical processes embedded in the model, we found agreement between simulated and measured ice number concentrations in most of the simulations, in contrast with previous modeling studies of Arctic mixed-phase clouds, which typically show a large discrepancy when IN are treated prognostically and constrained by measurements.

**Citation:** Avramov, A., et al. (2011), Toward ice formation closure in Arctic mixed-phase boundary layer clouds during ISDAC, *J. Geophys. Res.*, 116, D00T08, doi:10.1029/2011JD015910.

<sup>1</sup>Center for Climate Systems Research, Columbia University, New York, New York, USA.

<sup>2</sup>Now at Department of Earth, Atmospheric, and Planetary Sciences, Massachusetts Institute of Technology, Cambridge, Massachusetts, USA.

<sup>3</sup>NASA Goddard Institute for Space Studies, New York, New York, USA.

<sup>4</sup>Department of Meteorology, Pennsylvania State University, University Park, Pennsylvania, USA.

<sup>5</sup>Department of Electrical Engineering, Pennsylvania State University, University Park, Pennsylvania, USA.

<sup>6</sup>Science and Technology Branch, Environment Canada, Toronto, Ontario, Canada.

<sup>7</sup>Department of Atmospheric Sciences, University of Illinois at Urbana-Champaign, Urbana, Illinois, USA.

<sup>8</sup>Department of Atmospheric Sciences, Texas A&M University, College Station, Texas, USA.

<sup>9</sup>Flight Research Laboratory, National Research Council, Ottawa, Ontario, Canada.

### 1. Introduction

[2] Low-level mixed-phase stratus clouds are ubiquitous in the Arctic during much of the year. Unlike their midlatitude counterparts, in the Arctic mixed-phase clouds are quite long-lived. Surface observations indicate that they can persist for days and even weeks [Shupe *et al.*, 2006; Verlinde *et al.*, 2007] and maintain supercooled water even through the cold of the Arctic winter [Hobbs and Rangno, 1998]. Owing to their large horizontal extent, persistence, and the presence of the radiatively important liquid phase, mixed-phase clouds have a substantial impact on the surface energy budget in the Arctic [Shupe and Intrieri, 2004; Zuidema *et al.*, 2005].

[3] Although clouds have long been recognized as a vital part of various climate feedback mechanisms operating in the Arctic [Curry *et al.*, 1996], their representation in models remains poor. Recent model intercomparison studies [Klein *et al.*, 2009; Morrison *et al.*, 2009] reveal that even current state-of-the-art cloud-resolving models have serious

difficulties reproducing the observed cloud fields in observationally based case studies.

[4] A number of studies have suggested that interactions between the ice and liquid phase in models are a primary culprit in the significant underestimation of liquid water amounts in mixed-phase clouds. *Pinto* [1998] and *Harrington et al.* [1999] have explained the coexistence of liquid and ice in Arctic mixed-phase clouds through the balance between liquid water condensation, ice crystal depositional growth, and ice removal through sedimentation. Numerous modeling studies indicate that this balance is sensitive to ice crystal number concentration and thus, to the number concentration of heterogeneous ice nuclei (IN). The degree of sensitivity varies between models. In some studies very low IN concentrations are required to maintain the liquid phase, and moderate changes to IN concentrations lead to a substantial reduction of the liquid phase or rapid glaciation and dissipation of the simulated clouds [*Jiang et al.*, 2000; *Harrington and Olsson*, 2001; *Morrison et al.*, 2005; *Prenni et al.*, 2007; *Luo et al.*, 2008; *Avramov and Harrington*, 2010]. In other modeling studies [*Fridlind et al.*, 2007; *Morrison et al.*, 2008; *Fan et al.*, 2009], persistent mixed-phase layers are maintained despite IN concentrations two orders of magnitude greater. Persistence of the mixed-phase also depends on the large-scale advective tendencies of heat and moisture [*Jiang et al.*, 2000].

[5] Unresolved questions remain with respect to how ice is initiated in Arctic mixed-phase clouds and in ice clouds in general [*Cantrell and Heymsfield*, 2005]. Homogeneous freezing and well-established ice multiplication mechanisms [e.g., rime-splintering; *Hallett and Mossop*, 1974] typically can be ruled out as ice producing mechanisms since temperatures in Arctic mixed-phase clouds are often outside the relevant temperature ranges. Model simulations of Arctic mixed-phase clouds consistently fail to reproduce observed ice number concentrations. For instance, most of the modeling studies of the single-layer case from the Mixed-Phase Arctic Cloud Experiment (M-PACE) [*Verlinde et al.*, 2007] produced ice concentrations one to three orders of magnitude lower than observed [*Fridlind et al.*, 2007; *Prenni et al.*, 2007; *Luo et al.*, 2008; *Morrison et al.*, 2008; *Fan et al.*, 2009; *Solomon et al.*, 2009; *Avramov and Harrington*, 2010]. This problem is common for modeling studies of heterogeneous ice formation in mixed-phase clouds and stems from the fact that measured IN concentrations are often several orders of magnitude lower than measured ice concentrations [*Mossop*, 1970, 1985]. This unresolved discrepancy has motivated researchers to search for alternative nucleation modes or IN sources not detected by current IN techniques. *Morrison et al.* [2005] developed a conceptual model of Arctic mixed-phase clouds that explains cloud persistence and the continual production of ice through the rapid depletion of IN and a self-regulating negative feedback loop involving drop freezing associated with high concentrations of contact IN. *Fridlind et al.* [2007] examined a variety of ice nucleation mechanisms and demonstrated that two of them – IN formation from drop evaporation residuals (“evaporation IN” [*Rosinski and Morgan*, 1991]) and drop freezing during evaporation (“evaporation freezing” [*Cotton and Field*, 2002]), could produce liquid and ice amounts that match observational constraints. They also found that a surface source of conventional IN could also work. *Fan et al.* [2009]

report similar results with the same alternative nucleation mechanisms. They also point out that ice sublimation below the cloud also could be a significant source of recycled IN. The study of *de Boer et al.* [2010] suggests that undetected immersion IN might help to bridge the gap between measured IN and ice concentrations. Unfortunately, observational evidence constraining these mechanisms is rather sparse.

[6] A recent study by *Prenni et al.* [2009] presents a very different perspective. These authors reanalyzed Arctic IN measurements previously reported by *Rogers et al.* [2001] and *Prenni et al.* [2007] and compared them against corresponding ice concentration observations [*Gultepe et al.*, 2000; *McFarquhar et al.*, 2007]. Taking into account the uncertainty ranges for both types of measurements, the reanalysis showed that IN and ice concentrations are approximately equal if only large ice particles (with size greater than 125  $\mu\text{m}$ ) are considered. For smaller ice particles, IN and ice concentrations differ by two orders of magnitude. This difference was attributed to ice shattering artifacts [*Field et al.*, 2006; *Korolev et al.*, 2011]. Based on their findings, *Prenni et al.* [2009] infer that measured concentrations of large ice particles can be explained by heterogeneous ice formation mechanisms. Supporting this notion, *Eidhammer et al.* [2010] used parcel model simulations of a wave cloud to demonstrate the agreement between measured IN concentrations, model-predicted and observed concentrations of large ice.

[7] Here we test whether the same closure could be achieved in the context of Arctic mixed-phase clouds, namely that measured IN concentrations can explain ice formation in a new case study. Two days of the recent Indirect and Semi-Direct Aerosol Campaign (ISDAC) [*McFarquhar et al.*, 2011] appear to have the characteristics of an ideal testbed for this type of study: single mixed-layer stratocumulus deck, relatively high IN concentrations, a predominant ice crystal habit with low fall speed, and cloud base colder than  $-8^{\circ}\text{C}$ . We present results of large-eddy simulations with size-resolved microphysics for one of these days – April 8th. After describing the observations (Section 2) and the model used for simulations (Section 3), we provide the details of the simulations setup (Section 4). In Section 5 the model simulations are evaluated through extensive comparison with in situ observations and ground-based remote sensing measurements. In Section 6, we discuss and summarize our findings.

## 2. Case Description and Observations

[8] ISDAC was conducted in April of 2008 in the vicinity of Barrow, Alaska for the purpose of collecting observational data needed to advance our understanding of how cloud-aerosol interactions affect the microphysical and radiative properties of Arctic clouds [*McFarquhar et al.*, 2011]. For this experiment, the National Research Council (NRC) of Canada Convair-580 was instrumented for cloud in situ measurements by Environment Canada (EC) and NRC, and for aerosol measurements by EC and a number of other ISDAC partners [*McFarquhar et al.*, 2011]. Additional important information was provided by the NRC Airborne W- and X-Band (NAWX) radar and ground-based remote sensing observations at the Atmospheric Radiation

Measurement (ARM) program's Climate Research Facility (ACRF). Two of the ISDAC flights – flight 16 on April 8 and flight 31 on April 26 – are most suitable for the purposes of our study. Similar cloud systems were observed on both days: single mixed-layer low-lying stratocumulus decks with cloud base colder than the Hallet-Mossop splintering threshold of  $-8^{\circ}\text{C}$ . The relative simplicity of the cloud structure in these two cases facilitates the examination of the link between the tropospheric IN and in-cloud ice crystal number concentrations, without the complications associated with seeder-feeder effects in multiple layer systems or ice multiplication mechanisms. Here we focus only on the first case (8 April). Similar to measurements from a previous springtime campaign [Rogers *et al.*, 2001], for this case the observed mean IN concentrations were among the highest observed in the Arctic [cf. Prenni *et al.*, 2009], favoring the possibility of closure with respect to ice number concentrations. In addition, aircraft operations on that day were carried out in an immediate proximity to Barrow, allowing us to use the ACRF ground-based remote sensing instruments to further constrain the model simulations.

[9] A detailed inventory of the instruments on board the NRC Convair-580 aircraft is given by McFarquhar *et al.* [2011]. Here we provide only a brief summary of the instrumentation used to gather the in situ measurements used in this study. Cloud droplet number concentrations and liquid water content were measured by the Particle Measuring Systems (PMS) Forward Scattering Spectrometer Probe (FSSP-100) and the PMS Commonwealth Scientific and Industrial Research Organization (CSIRO) King probe. The FSSP-100 probe suffered from problems during ISDAC that resulted in an artificial broadening of the particle size distributions; comparisons with the Droplet Measurement Technologies (DMT) Cloud Droplet Probe (CDP), however, revealed that the FSSP-100 yielded reasonable total droplet concentrations. Since the CDP probe was not operational during the flight of April 8 we use the FSSP-100 droplet number concentrations. The PMS 2D-C, PMS 2D-P, and Stratton Park Engineering Company (SPEC) 2D-S optical array probes were used to determine ice particle size distributions, number concentrations and ice water content. Images from the SPEC Cloud Particle Imager (CPI) were used to assist in ice particle habit identification. IN concentrations were measured by the Texas A&M Continuous Flow Diffusion Chamber (CFDC). We also use reflectivities from the NRC NAWX radar on board the Convair-580 as well as reflectivities and mean Doppler velocities from the Ka-band Millimeter Wavelength Cloud Radar (MMCR) located at the ACRF site at Barrow.

[10] Special tips were installed on the 2D-C probe, which significantly mitigate of the effect of ice crystal shattering on measurements [Korolev *et al.*, 2011]. Filtering of shattering events was conducted with the help of arrival time anti-shattering algorithms [Field *et al.*, 2006]. To reduce uncertainties associated with depth-of-field, image digitization and shattering, we consider only ice particles with maximum dimension greater than  $100\text{ }\mu\text{m}$  for all size distributions and quantities computed from the size distributions. For the 2D-S, another probe used here at those particle sizes, Lawson [2011] report that arrival-time filtering algorithms are sufficient to remove artifacts down to much smaller sizes. There is still considerable uncertainty

with regard to the size range and environmental conditions where shattering is important and also the degree to which filtering algorithms can remove the shattered particles. The effectiveness of the removal of shattering artifacts is a subject of current debate, and definitive statements at this point are beyond the scope of this study. Given present understanding, we consider a threshold of  $100\text{ }\mu\text{m}$  to be a reasonable choice.

[11] On 8 April the North Slope of Alaska (NSA) was under the influence of a deep high-pressure system that created favorable conditions for development of a persistent single-layer stratocumulus deck over the NSA and adjacent Beaufort Sea. As the high-pressure system slowly moved northward, closer to Barrow, the cloud top height gradually decreased. The time evolution of the cloud layer over Barrow as seen by the MMCR is shown on Figure 1.

[12] Two research flights were conducted on 8 April. Here we focus on the second flight for that day (flight 16), when the extensive stratocumulus deck was sampled over the ocean west of Barrow. After several spiral profiles over the ACRF site, constant altitude legs below, above and through the cloud deck, the NRC Convair-580 executed a series of porpoising maneuvers consisting of ramped ascents and descents through the cloud layer between 22:27–23:00 UTC (Figure 2).

[13] Consistent with Figure 1, the cloud top height gradually decreased from about 1200 m at the beginning (most westward point) to about 800 m at the end (most eastward point) of the 180-km long porpoising leg. Cloud top temperatures (not shown) accordingly increased from  $-15^{\circ}\text{C}$  to  $-12^{\circ}\text{C}$ . Vertical soundings, constructed from aircraft measurements, showed that the depth of the mixed-phase layer varied from 100 to 350 m, generally decreasing from west to east. The liquid water content (LWC) in each individual profile was nearly adiabatic and the cloud top value varied from about 0.1 to about  $0.3\text{ g m}^{-3}$  (Figure 2). FSSP-100 cloud droplet concentrations varied between 100 and 200 per  $\text{cm}^{-3}$ , showing a substantial increasing trend from west to east during the porpoising leg. The ice crystal number concentrations ( $N_i$ ) shown on Figure 2 are derived from the composite ice particle size distributions measured by 2D-S and 2D-P probes. Concentrations of ice particles larger than  $100\text{ }\mu\text{m}$  were generally lower than those measured during M-PACE [cf. McFarquhar *et al.*, 2007] and rarely exceeded  $1\text{ L}^{-1}$ .  $N_i$  of ice larger than  $100\text{ }\mu\text{m}$  averaged over the duration of the porpoising legs was about  $0.4\text{ L}^{-1}$ . Because of technical problems during this flight no reliable bulk measurements of ice water content (IWC) were available. However, using data from other ISDAC flights when both Nevzorov Deep Cone and Cloud Spectrometer and Impactor (CSI) probes were operational, it was determined that the Baker and Lawson [2006] method, which relates the mass of a particle to its (randomly oriented) cross-sectional area, provides good agreement between the mass estimated from the size distributions and that measured by the bulk probes, hereafter referred to as the habit-independent estimate of IWC. Accordingly, in Figure 2 we show the 30-s averages of the IWC computed using the Baker and Lawson [2006] method. The IN concentrations detected by the CFDC were also highly variable, ranging from below the detection threshold of  $0.1\text{ L}^{-1}$  to above  $20\text{ L}^{-1}$ . Although IN concentrations were measured during most of the flight duration,

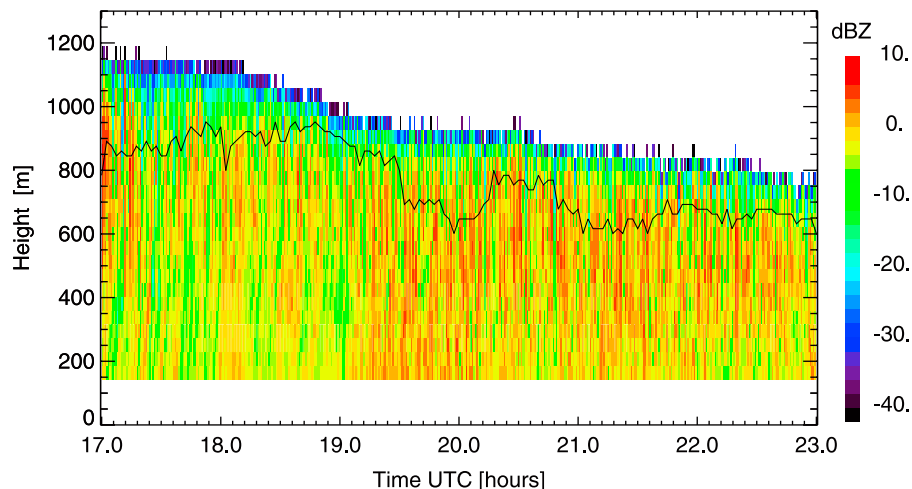


**Figure 1.** Time series of MMCR reflectivity at Barrow, Alaska on 8 April 2008. Cloud base as retrieved through the Active Remote Sensing of Clouds (ARSCL) algorithm [Clothiaux *et al.*, 2000] is shown with a black solid line. Given a mean horizontal wind speed of about  $9 \text{ m s}^{-1}$  in the boundary layer (from the Barrow sounding at 17.34 UTC), these six hours are equivalent to about 200 km of horizontal distance. For reference, ISDAC flight 16 started at 19:54 and ended at 23:36 UTC on the same day.

here we only use IN data when the CFDC was sampling ambient air (Figure 2). The IN concentrations above the cloud layer averaged between  $7.3$  and  $9.8 \text{ L}^{-1}$  (depending on whether or not zeros are included in the average) much larger than the average IN concentration during M-PACE [Prenni *et al.*, 2007] and similar to that measured during springtime in the Arctic [Rogers *et al.*, 2001]. Unfortunately, no usable IN data below or within the cloud layer are available for this flight. We note that the IN measurements during this flight were all collected below water saturation, indicating that the measured IN were active in the depositional mode. In contrast, during M-PACE depositional freezing was found to be unproductive; that is, most IN were measured above saturation [Prenni *et al.*, 2009]. IN data from other ISDAC flights, when the CFDC was operated both below and above water saturation, suggest that IN concentrations sampled on flight 16 may therefore have been underestimated by up to an order of magnitude [McFarquhar *et al.*, 2011].

[14] Analysis of ice crystal habit observations using an automated habit classification procedure [Korolev and Sussman, 2000] indicates the predominance of dendritic crystal shapes at all levels during this flight (Figure 3). Manual inspection of CPI, 2D-C and 2D-P images reveals no evidence of riming but much evidence of substantial aggregation at larger sizes (Figure 4). This contrasts with the single-layer M-PACE case in which many irregular and heavily rimed ice particles were observed [McFarquhar *et al.*, 2007; Fridlind *et al.*, 2007].

[15] In addition to the in situ observational data discussed above, reflectivity and mean Doppler velocity fields from the NAWX X-band radar and the MMCR are used to further constrain model simulations. The gradual decline of cloud top heights observed on the flight track, together with the almost 200 km distance to Barrow, raises the question of how relevant the MMCR observations from Barrow are to the in situ sampled cloud fields. To partially address this issue we compare the radar reflectivities below the cloud top measured by the NAWX radar between 22:30 and

23:00 UTC with those from the MMCR, collected at Barrow during two time periods – 17:00–17:30 UTC and 22:30–23:00 UTC. Frequency distributions of NAWX and MMCR mean reflectivity show reasonable agreement during both time periods (Figure 5), suggesting similar cloud properties. Here we use only MMCR data obtained in the “stratus” mode [Kollias *et al.*, 2007]. The MMCR radar reflectivities were corrected by subtracting 9.8 dBZ from the reported values because of a known calibration offset [Protat *et al.*, 2011]. Quality analysis of the NAWX data was performed using the NRC cloud mask, thus eliminating all pixels identified as noise or ground contaminated.

[16] Ice crystal fall speeds represent a major source of uncertainty in model simulations. Here we use the MMCR reflectivity and Doppler velocity spectra to estimate reflectivity-weighted ice fall speeds in the cloud layer, following Rambukkange *et al.* [2011]. This technique uses cloud droplets as a tracer to determine the contributions of vertical winds to the mean Doppler velocity and, hence, the reflectivity-weighted ice fall speed. Retrieved ice fall speeds and vertical winds are shown on Figure 6. The uncertainty of this method has been estimated to be about  $0.1 \text{ m s}^{-1}$ , but neglecting turbulent broadening of the Doppler spectra [Shupe *et al.*, 2008b] introduces a systematic high bias of  $0.2\text{--}0.3 \text{ m s}^{-1}$  in the air motion.

### 3. Model Description

[17] The model we use in our simulations is the Distributed Hydrodynamic Aerosol and Radiative Modeling Application (DHARMA). DHARMA consists of a large-eddy simulation (LES) dynamical core [Stevens *et al.*, 2002] with a dynamic Smagorinsky subgrid-scale turbulence model [Kirkpatrick *et al.*, 2006], coupled with a (size-resolved) bin microphysics model [Ackerman *et al.*, 1995, 2004; Fridlind *et al.*, 2007] and a two-stream radiative transfer model with 44 wavelength bands [Toon *et al.*, 1989]. A more detailed description of the model is given

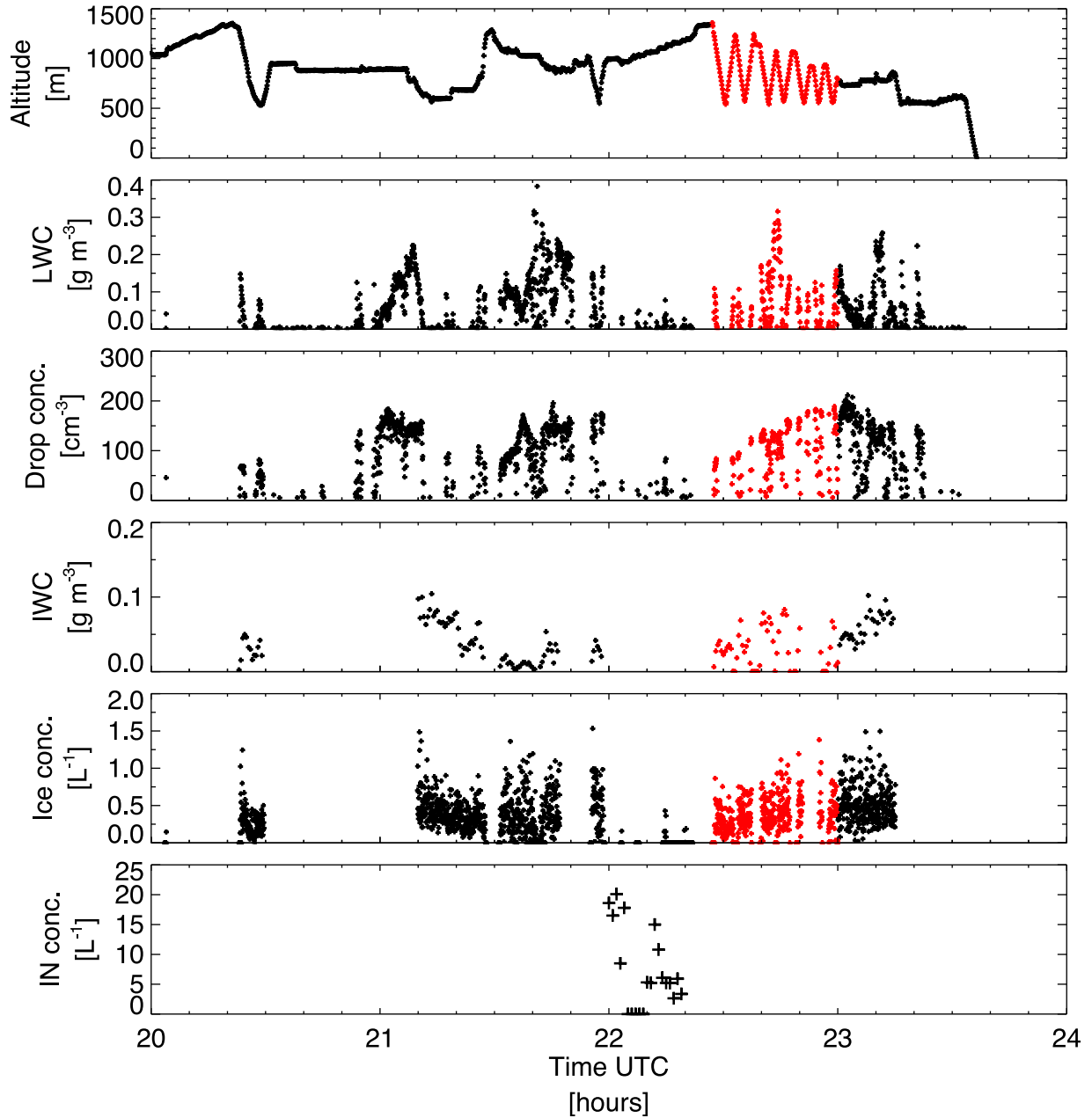


**Figure 2.** Time series of in situ measurements during ISDAC Flight 16: (top to bottom) aircraft altitude, liquid water content (LWC) from the King hotwire probe, cloud droplet number concentration from the FSSP-100, habit-independent ice water content (IWC) derived from size distributions measured by the 2D-S and 2D-P (see text), ice number concentration from the 2D-S and 2D-P, and IN concentration measured by CFDC. IN concentrations shown only when CFDC was sampling through the ambient inlet. The time period selected for comparisons with model simulations is shown in red.

elsewhere [Ackerman *et al.*, 1995, 2004; Fridlind *et al.*, 2007, 2011]; here we discuss only some aspects specific to our simulations.

[18] To test the hypothesis that observed IN concentrations can account for ice formation in this Arctic mixed-phase cloud deck, we assume that all ice is formed heterogeneously only through well-established ice formation mechanisms. Since cloud base temperature here is colder than  $-8^{\circ}\text{C}$  and no significant amount of riming was observed, we omit droplet-ice collisions and all ice-multiplication processes. All four

standard heterogeneous nucleation modes are explicitly present in the model: condensation, deposition, contact and immersion freezing. A 10-element grid of decreasingly accessible IN is used to keep track of the prognostic IN. The IN in each grid cell are arranged in ten bins from most to least easily nucleated, depending on the ambient temperature and supersaturation [Fridlind *et al.*, 2007]. The IN can be activated in any mode provided the necessary conditions are met. We use the same temperature and supersaturation ranges for each nucleation mode as listed in Table 1 of



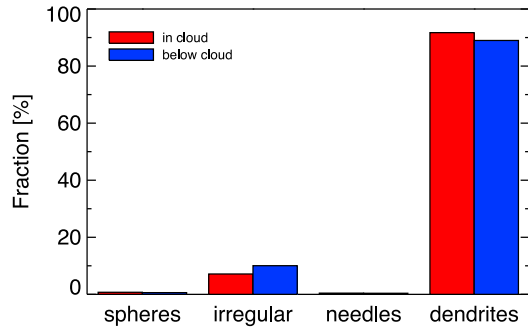


**Figure 3.** Fraction of different habits in 4-s samples collected within cloud and below cloud base between 22:30 and 23:00 UTC on 8 April. Cloud base height is determined using a threshold value of cloud droplet concentration equal to  $5 \text{ cm}^{-3}$ .

*Fridlind et al.* [2007], with the only difference being that the deposition nucleation temperature threshold is decreased from  $-10^\circ\text{C}$  to  $-5^\circ\text{C}$ , to be consistent with the widely used *Meyers et al.* [1992] parameterization, though the change is of no consequence here. Many models [e.g., *Morrison et al.*, 2005; *Prenni et al.*, 2007] make the assumption that contact IN are not accessible in any other mode and use a separate parameterization for contact IN [e.g., *Meyers et al.*, 1992]. Adopting a similar approach here would introduce an additional source that would be unconstrained by the CFDC measurements and thus in conflict with our hypothesis. Our assumption is also consistent with laboratory measurements showing some aerosols to act as both contact and immersion IN [Fornea et al., 2009]. The IN are treated prognostically in our simulations: IN concentrations in 10 separate bins are subject to advection, subsidence, diffusion, and depletion. No IN sources into the boundary layer other than entrainment from aloft are considered.

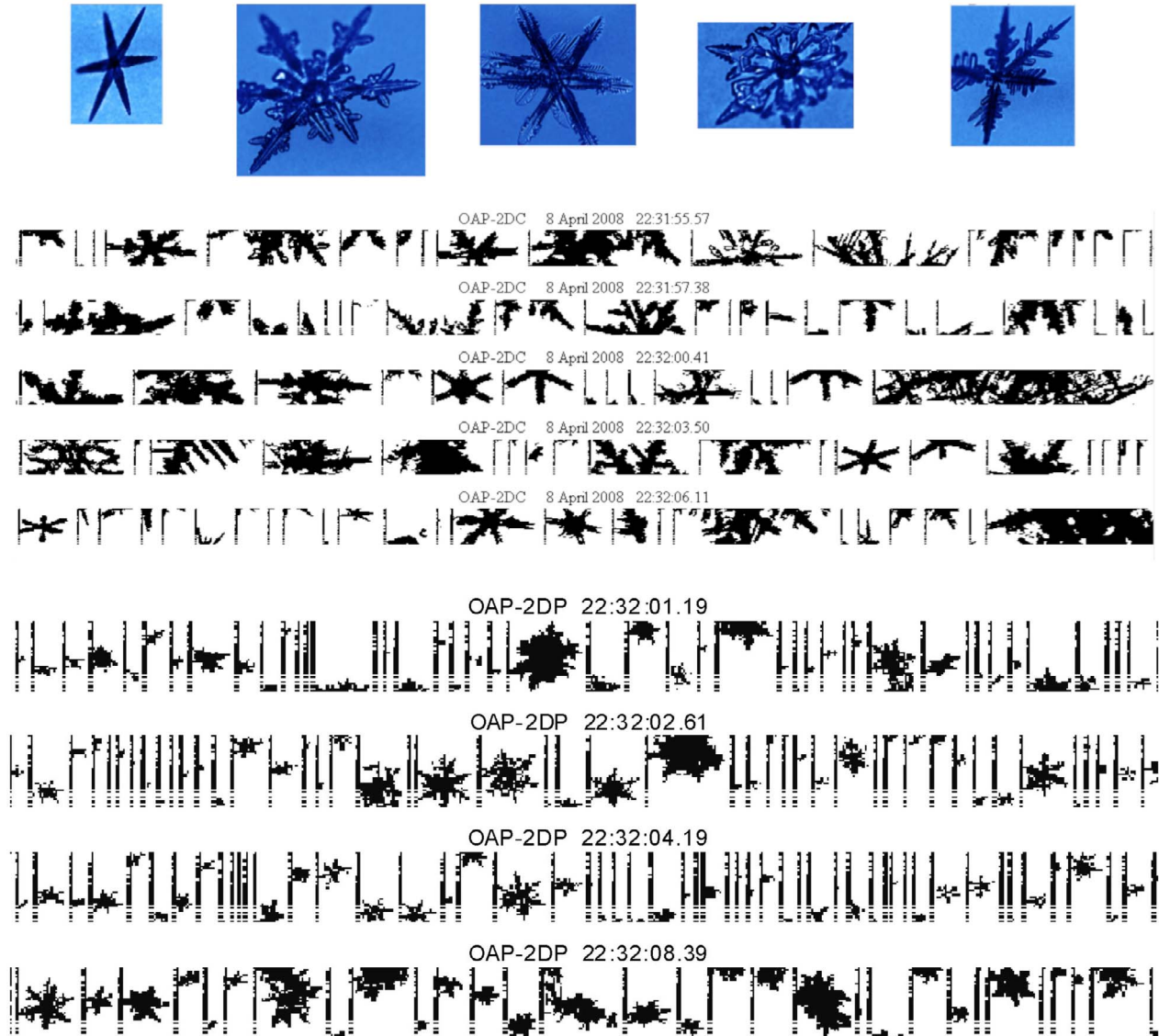


**Figure 4.** Representative (top) CPI, (middle) 2D-C, and (bottom) 2D-P images collected between 22:30 and 23:00 UTC on 8 April. The maximum dimensions of the ice crystals on the CPI images is about 1.2 mm and the vertical size of each row of 2D-C and 2D-P images is 0.8 and 6.4 mm, respectively.

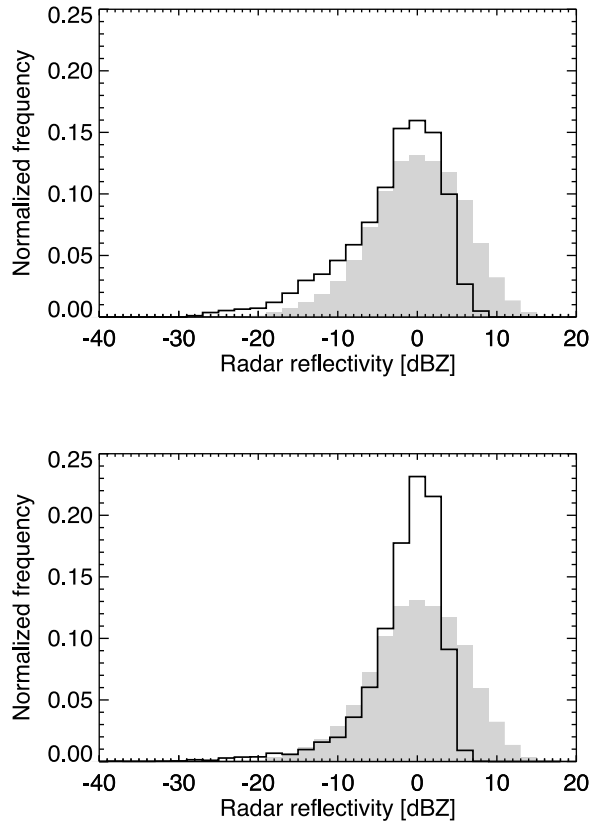


**Figure 5.** Measured NAWX X-band (shaded) and MMCR Ka-band (solid black line) equivalent radar reflectivities for (top) 17:00–17:30 UTC and (bottom) 22:30–23:00 UTC time periods.

[19] DHARMA has the option of any number of size-resolved ice categories. Consistent with observations, we use two categories configured to represent dendritic pristine ice crystals and snow aggregates composed of dendrites. Pristine ice crystals (hereafter dendrites) are formed by one of the nucleation modes discussed above and grow by vapor deposition. Aggregates form through collisions between pristine ice crystals and grow by vapor deposition and aggregation. Ice particle properties in each mass bin are specified by the following three parameters: maximum dimension ( $D$ ), maximum projected area and aspect ratio. Since these parameters can vary significantly even within the same ice habit, we select from the literature relations that define the extremes in mass range for a given size. We define high density and low density versions of both pristine ice and aggregates, and run simulations using the low or high density versions for both ice categories. In the case of dendrites, we use mass- and area-dimensional relations for P1d (low density) and P1c (high density) crystals from Mitchell [1996]. For high density aggregates we use “aggregates of thin plates” [Mitchell and Heymsfield, 2005] and low density aggregates are aggregates composed of P1e crystals [Kajikawa, 1989]. In addition, we concatenate several dimensional relations for each category. Both dendrite and aggregate classes with  $D < 10 \mu\text{m}$  are treated as ice spheres, and aggregates with  $D < 90 \mu\text{m}$  use the dimensional relation for the dendrite crystal. We do not expect aggregation to occur at such small sizes (and as we show later in section 5,

it does not occur in our simulations). However, ice crystal properties need to be specified in each of the model size bins, even though they are somewhat contrived at the extreme ends of the size ranges. The coefficients in mass- and area-dimensional relations and their size ranges are listed in Table 1. Since no area-dimensional data was available for the low density aggregates, the coefficients in the area-dimensional relation were determined by trial-and-error until calculated fall speeds were brought into agreement with those in Kajikawa [1989]. Because of the differences in the mass-dimensional relations, the low density ice crystals will experience larger depositional growth rates, increasing both their mass and size faster than their high density counterparts.

[20] The aspect ratio ( $\alpha$ ) is approximated based on ice crystal geometry:

$$\alpha = \max\left\{\frac{m}{\rho_i A_e D}, \alpha_{\min}\right\}, \quad (1)$$

where  $m$  is mass,  $\rho_i$  is bulk density, assumed  $0.9 \text{ g cm}^{-3}$  for pristine ice and  $0.6 \text{ g cm}^{-3}$  for aggregates of dendrites [e.g., Böhm, 1989],  $A_e$  is the area projected to the flow, and  $\alpha_{\min}$  is 0.04 in the case of dendrites [e.g., Böhm, 1992a; Hashino and Tripoli, 2011a, 2011b]. For aggregates  $\alpha_{\min}$  is set to 0.1, taking into account the aspect ratio of the component crystals and assuming they stick on their basal surfaces. This value is not well known but evidently does not impact

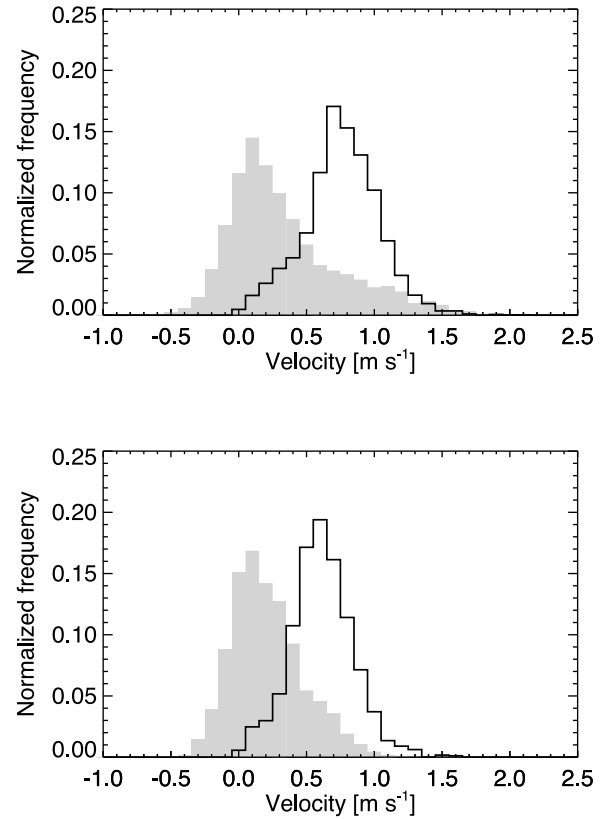


**Figure 6.** Retrieved vertical air velocity (shaded) and reflectivity-weighted ice crystal fall speed (solid black line) inside the cloud layer for (top) 17:00–17:30 UTC and (bottom) 22:30–23:00 UTC. Motion toward the ground is recorded as a positive velocity here.

**Table 1.** Ice Particle Properties

Habit Type	$D$ Range (cm)	$m$ - $D$ $a^a$	$m$ - $D$ $b^a$	$A$ - $D$ $c^a$	$A$ - $D$ $d^a$	Reference Sources <sup>b</sup>
<i>Low Density Dendrites</i>						
spheres	$<1 \times 10^{-3}$	0.4814	3.0	0.7854	2.0	-
small dendrites	$1 \times 10^{-3} - 9 \times 10^{-3}$	0.00583	2.42	0.24	1.85	M96
large dendrites	$>9 \times 10^{-2}$	0.00027	1.67	0.11	1.63	M96
<i>High Density Dendrites</i>						
spheres	$<1 \times 10^{-3}$	0.4814	3.0	0.7854	2.0	-
small dendrites	$1 \times 10^{-3} - 9 \times 10^{-3}$	0.00583	2.42	0.24	1.85	M96
large dendrites	$>9 \times 10^{-2}$	0.000516	1.80	0.21	1.76	M96
<i>Low Density Aggregates</i>						
spheres	$<1 \times 10^{-3}$	0.4814	3.0	0.7854	2.0	-
small dendrites	$1 \times 10^{-3} - 9 \times 10^{-3}$	0.00583	2.42	0.24	1.85	M96
aggregates	$>9 \times 10^{-2}$	0.000482	1.97	0.27 <sup>c</sup>	2.10 <sup>c</sup>	K89
<i>High Density Aggregates</i>						
spheres	$<1 \times 10^{-3}$	0.4814	3.0	0.7854	2.0	-
small dendrites	$1 \times 10^{-3} - 1.9 \times 10^{-2}$	0.00583	2.42	0.24	1.85	M96
aggregates	$>1.9 \times 10^{-2}$	0.00145	1.80	0.2285	1.88	MH05

<sup>a</sup>Values of  $a$ ,  $b$ ,  $c$ , and  $d$  in  $m = aD^b$  and  $A = cD^d$ , where  $m$  is mass in g,  $D$  is maximum dimension in cm, and  $A$  is maximum projected area in cm<sup>2</sup>.

<sup>b</sup>K89 = Kajikawa [1989], MH05 = Mitchell and Heymsfield [2005], M96 = Mitchell [1996].

<sup>c</sup>See text.

growth rates appreciably here (see section 5.5), and calculated fall speeds are consistent with relevant measurements. Figure 7 illustrates the dimensional relations of all ice types used here.

[21] Previous modeling studies of Arctic mixed-phase clouds have documented the importance of habit-dependent ice growth and sedimentation rates in the simulations of these clouds. Accordingly, here we describe some of the details of their parameterization in our simulations. To approximate the impact of crystal geometry on vapor deposition and sublimation rates, shape factors ( $S$ ) for dendrite crystals are calculated assuming stellar crystals [Westbrook et al., 2008] as

$$S = C/a = 0.58(1 + 0.95\alpha^{0.75})(1 - 0.38e^{-4.7A'}), \quad (2)$$

where  $C$  is capacitance,  $a$  is half the maximum dimension, and  $A'$  is the arm aspect ratio. The geometry of a six-arm stellar crystal leads to

$$A' = \frac{8A_e}{3a^2}, \quad (3)$$

while for aggregates we assume  $S = 0.5$  [Westbrook et al., 2008], as seen in Figure 7.

[22] DHARMA uses an integrated treatment of cloud particle fall speeds and gravitational collection rates [Böhm 1989, 1992a, 1992b, 1992c, 1994, 1999, 2004]. In this treatment, fall speeds and collection rates of particles with arbitrary shapes are based on four parameters: particle mass, maximum dimension, maximum projected area and aspect ratio. Central to this approach is the relation between the particle Best or Davies number ( $X$ ) and its Reynolds number ( $Re$ ):

$$X = C_D Re^2, \quad (4)$$

where  $C_D$  is the drag coefficient. Laboratory measurements of List and Schemenauer [1971] show that  $C_D$  is sensitive to irregularities of the particle cross-sectional area normal to the flow. Based on their results Böhm [1989] proposed a modified drag coefficient ( $C_{De}$ ) that accounts for such deviations:

$$C_{De} = C_D \left( \frac{A}{A_e} \right)^k, \quad (5)$$

and correspondingly modified Best number:

$$X_e = C_{De} Re^2. \quad (6)$$

In these equations  $A$  is the circumscribed particle area of the particle, and  $k$  is an empirical coefficient.

[23] Böhm [1989] found that  $k = 3/4$  provides the best fit to List and Schemenauer [1971] data. Heymsfield and Westbrook [2010] demonstrated that equation (4) of Mitchell [1996] leads to a significant overestimation of the fall speeds of particles with open geometry – stellars, dendrites, needles and low density aggregates. Using laboratory and field data for a variety of particle shapes they proposed a correction similar to equation (5) and found that  $k = 1/2$  provides optimal agreement with their data. Here we adopt their value when calculating fall speeds and gravitational collection rates; resulting fall speeds are shown on Figure 7. Typical retrieved reflectivity-weighted fall speeds (see Figure 6) generally lie within the range of fall speeds for the low and high density aggregate types when considering retrieval uncertainty.

[24] Collision efficiencies for all combinations (liquid-liquid, liquid-ice, ice-ice) are calculated following Böhm [1999]. We use size-dependent coalescence efficiencies for water droplets [Beard and Ochs, 1984]. Since no rimed crystals were evident in the in situ measurements, the coalescence efficiency for liquid-ice collisions was zeroed. Ice-ice coalescence efficiency is not well known. Field



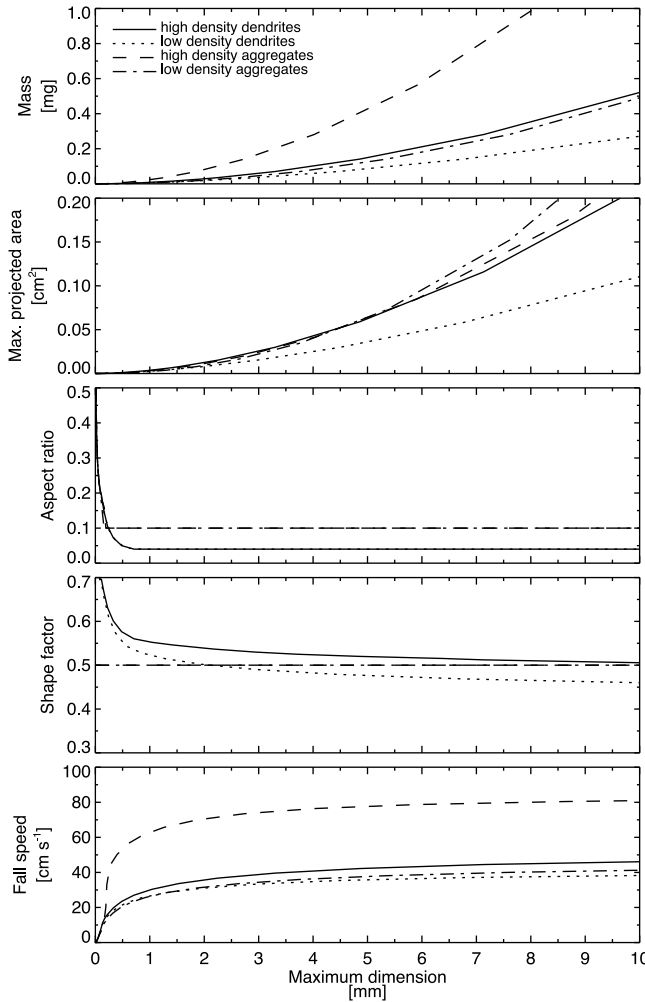


**Figure 7.** (top to bottom) Particle mass, maximum projected area, aspect ratio, shape factor and fall speeds for each ice category. Fall speeds in this figure are computed for  $T = 257$  K and  $p = 900$  mb, which approximately corresponds to the top of the cloud layer.

measurements suggest that ice aggregation is habit-dependent with dendrites having the greatest potential for aggregation [Raubert, 1987]. Mitchell [1988] estimated the temperature-dependent probability of aggregation for dendritic crystals in the temperature range between  $-17^{\circ}\text{C}$  and  $-12.5^{\circ}\text{C}$  to be unity. Since cloud temperatures for this case fall within that range, here we assume coalescence efficiency for ice-ice collisions of unity.

#### 4. Simulation Setup

[25] Simulations presented here use a three-dimensional domain size of  $3.2 \times 3.2 \times 1.5$  km with uniform grid spacing of 50 m horizontally, and 15 m vertically. We use periodic lateral boundary conditions and a sponge layer with a timescale decreasing to 100 s in the upper 250 m of the domain. The dynamic time step is 5 s, unless the advective flow Courant number exceeds 0.8. Horizontal winds are nudged toward their initial profile with a 1-h time scale. To minimize errors associated with advection, the computa-

tional domain is translated with mean boundary layer winds of 8.5 and  $3 \text{ m s}^{-1}$  from the east and south. The surface skin temperature is specified at 264.7 K (from National Oceanic and Atmospheric Administration U.S. Climate Reference Network surface measurements), a surface roughness length of 0.4 mm is assumed [Persson *et al.*, 2002] and surface turbulent fluxes are computed from Monin-Obukhov similarity theory using the dimensionless profiles of *Businger et al.* [1971] with a Prandtl number of unity and von Karman coefficient of 0.41. The surface flux of moisture is computed assuming 100% relative humidity with respect to ice at the surface skin temperature. Computed surface sensible and latent heat fluxes, averaged over the last three hours of the simulations discussed in Section 5.4, are about  $1.0 \text{ W m}^{-2}$  and  $1.2 \text{ W m}^{-2}$  respectively.

[26] We use 32 successively mass-doubling bins to represent each of the number size distributions for water droplets, dendrites and aggregates. The mass of the smallest bin in all three grids is that of a droplet with  $D = 2 \text{ }\mu\text{m}$  and the number of bins satisfies the requirement that the concentration of particles in the largest bin is never more than that in the preceding bin. Aerosols are treated diagnostically and are initialized with a lognormal size distribution with geometrical standard deviation  $\sigma_g = 1.4$ , mean radius  $r_g = 0.094 \text{ }\mu\text{m}$  and total number concentration  $N_a = 165 \text{ cm}^{-3}$ , which is based on a preliminary version of aerosol measurements from the aircraft. The final version of those data is similar ( $\sigma_g = 1.43$ ,  $r_g = 0.1 \text{ }\mu\text{m}$ ,  $N_a = 171.7 \text{ cm}^{-3}$ ) and includes a coarse mode ( $\sigma_g = 2.35$ ,  $r_g = 0.55 \text{ }\mu\text{m}$ ,  $N_a = 5 \text{ cm}^{-3}$ ) but model results are not sensitive to these changes, as discussed below. We assume dry aerosol mass to be pure ammonium bisulfate as in work by Fridlind *et al.* [2007].

[27] The model is initialized using the Barrow 17:34 UTC balloon sounding (Figure 8). Since the sounding is unsaturated despite the presence of cloud at that time (see Figure 1), to readily develop a cloud layer in the simulations we moistened the sounding by assuming that the initial water vapor mixing ratio in the upper portion of the boundary layer is equal to its value at the inflection point in the relative humidity profile at a height of about 500 m. No hydrometeors are initially present in the model.

[28] The profiles of large-scale horizontal advective tendencies of temperature and water vapor and large-scale vertical winds from National Centers for Environmental Prediction (NCEP) reanalysis and variational analysis based purely on European Centre for Medium-Range Weather Forecasting (ECMWF) reanalysis [Zhang and Lin, 1997; Zhang *et al.*, 2001] are in substantial disagreement, not only in magnitude but also in sign (not shown). Lacking guidance, we neglect large-scale horizontal advective tendencies for the 6-h duration of our simulations. The large-scale vertical winds from reanalysis for the time period of flight 16 range from ascent to modest subsidence rates of no more than about  $0.6 \text{ cm s}^{-1}$  at cloud top altitude. Given the 250 m descent of cloud top altitude starting at 1200 m over 6 h from the cloud radar over Barrow (Figure 1), which is  $1.1 \text{ cm s}^{-1}$  of descent, we impose large-scale subsidence profile in our simulations based on that descent rate according to  $w_{sub} = -D_h z$ , where  $z$  is altitude and  $D_h = 9.1 \cdot 10^{-6} \text{ s}^{-1}$  is the horizontal wind divergence derived using  $w_{sub} = 1.1 \text{ cm s}^{-1}$  and  $z = 1200 \text{ m}$ . We note that this interpretation likely represents an upper limit on the actual large-scale subsidence. An

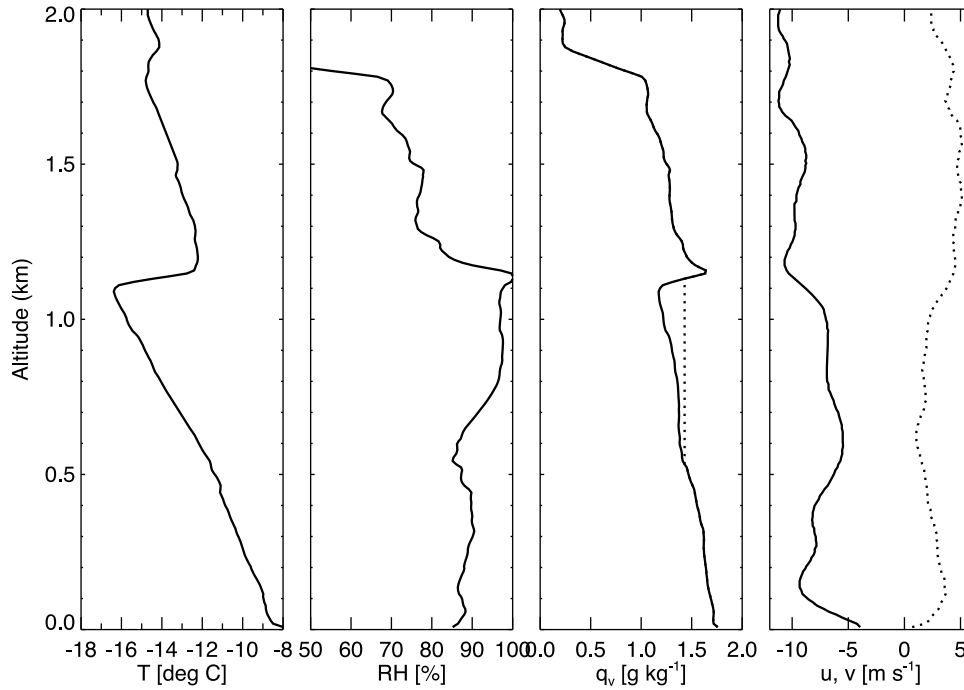


**Figure 8.** Atmospheric profiles of (left to right) temperature, relative humidity, water vapor mass mixing ratio, and zonal and meridional winds (solid and dotted lines, respectively) from Barrow radiosonde launched at 17:30 UTC on 8 April 2008. Initial water vapor profile used for the simulations is idealized in upper half of boundary layer as shown by dotted line in third panel (see text for explanation).

alternative interpretation is to consider the descending cloud top altitude at Barrow a consequence of the horizontal advection of a sloped inversion height combined with large-scale subsidence. By ignoring any large-scale horizontal advection, the subsidence used in the simulations is most likely overestimated. A sensitivity run testing the impact of such an overestimation is discussed in Section 5.5.

[29] To set the upper boundary condition on the radiative transfer model, the computed downwelling longwave flux just above cloud top was set to match a value of  $160 \text{ W m}^{-2}$ , estimated from aircraft radiative flux measurements above the boundary layer in which the pitch and roll were both less than  $5^\circ$ .

## 5. Results

[30] We organize the simulations presented in this section as follows. First, simulations are performed with two dendrite types using observed IN concentrations. Then simulations with observed and enhanced IN concentrations are run using each dendrite type together with low or high density aggregates. Finally, sensitivity to the shape of the initial IN profile is explored in simulations using dendrites together with aggregates.

[31] Simulations presented in the following subsections are evaluated through comparisons with observed vertical profiles and with in- and sub-cloud averages of ice particle size distributions. In addition, simulated radar reflectivities and mean Doppler velocities are compared to those measured by the MMCR and NAWX radar, similar to other studies [Lawson and Zuidema, 2009; van Diedenhoven et al., 2009; Fan et al., 2009; Fridlind et al., 2011]. The last three of

those studies used the Quickbeam software package [Haynes et al., 2007] to compute radar reflectivity and mean Doppler velocity fields. Botta et al. [2010], however, have demonstrated that the bulk sphere approximations, similar to the “soft sphere” model used in Quickbeam, can underestimate the backscattering cross-sections of ice particles larger than about 2 mm by up to 20 dB at 35 GHz. Accordingly, here we use the more accurate generalized multiparticle Mie (GMM) [Botta et al., 2010] method, which explicitly accounts for the geometry of the ice particles. Both individual dendrites and aggregates are assumed to be oriented horizontally; the dendrites within aggregates are randomly oriented within a 25 degree standard deviation canting angle. The details of this method as applied to the simulations presented here are described by Botta et al. [2011].

[32] We begin with simulations using dendrites only.

### 5.1. Simulations With Dendrites

[33] In the simulations presented in this subsection the initial IN concentration above the inversion capping the boundary layer is set to  $10 \text{ L}^{-1}$ , corresponding to the average IN concentrations measured there. Since no reliable IN data in and below the mixed-phase cloud layer are available for this case, the initial IN concentration below the inversion is set to  $1 \text{ L}^{-1}$ , roughly reflecting measured ice concentrations.

[34] As seen in Figure 9, liquid water path (LWP) shows little variation, slowly increasing from about  $40 \text{ g m}^{-2}$  to less than  $50 \text{ g m}^{-2}$  over the six-hour simulations. Average ice water path (IWP), after a surge during the first hour, gradually decreases to about  $2 \text{ g m}^{-2}$  by the end of the simulations. Similar to IWP, average ice crystal number concentrations rapidly increase in the beginning of the simulations

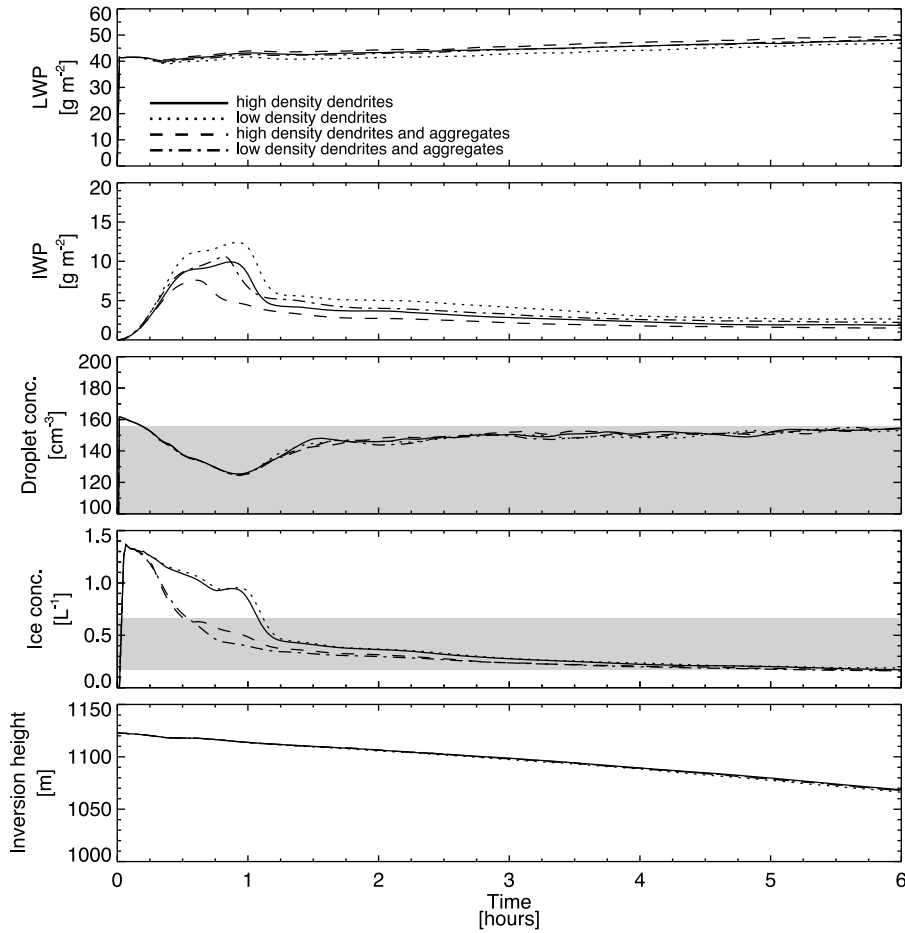


**Figure 9.** Time series of domain averaged (top to bottom) liquid water path (LWP), ice water path (IWP), droplet number concentration, ice crystal number concentration and inversion height in simulations with dendrites only and with dendrites and aggregates. The simulations depicted are initialized with IN concentrations of  $1 \text{ L}^{-1}$  within the boundary layer and  $10 \text{ L}^{-1}$  above assuming high density or low density dendrites with or without aggregates (see legend). Shading denotes 15th–85th-percentile range of observations. Average droplet concentrations are weighted by the mass mixing ratio of liquid water, ice crystal concentrations only include particles with maximum dimension exceeding  $100 \mu\text{m}$  and are averaged over grid cells with more than  $0.001 \text{ L}^{-1}$  of such ice, and inversion height is defined as the average altitude where the liquid-ice potential temperature is  $268 \text{ K}$ , which always corresponds to the top of the boundary layer here.

owing to the abundance of IN inside the mixed-phase cloud layer. After these initial IN are depleted, the dominant source of IN is entrainment from above. This source is inadequate to maintain the ice concentrations at their early levels and they show a steady decline to about  $0.2 \text{ L}^{-1}$  at the end of the simulations without reaching a steady state. Cloud droplet concentrations are relatively constant after dynamics has spun up during the first hour or so.

[35] Profiles of cloud properties are compared with the in situ observations in Figure 10. Simulated quantities are sampled from the last three hours of the simulations. Since observed cloud top heights varied considerably, the measured profiles are normalized with respect to the cloud top height in each of the ascending and descending profiles shown in Figure 2. Similarly, the profiles of the simulated quantities are normalized with respect to simulated cloud top height (a threshold value of cloud droplet concentration of  $5 \text{ cm}^{-3}$  is used in determining cloud top and cloud base).

As noted above, the IN concentration profiles show that most of the boundary layer is almost completely depleted of IN after the first three hours of simulation time. In simulations with either low or high density dendrites, ice number concentrations are commonly underestimated within the cloud layer but show better agreement with observations just below cloud top and at the lowest altitudes sampled by the aircraft. On the other hand, cloud droplet concentrations and LWC appear to be significantly overestimated. The apparent overestimation is likely related to the averaging and normalization procedures applied here. For a property with strong height dependency, like LWC, height normalization would produce a reasonable profile were cloud thickness varying in concert with the cloud top height. As Figure 1 illustrates, this may not be the case here since variations in retrieved cloud top and cloud base altitudes are comparable in magnitude but not well correlated. Similarly, the observed average droplet number concentrations in Figure 10

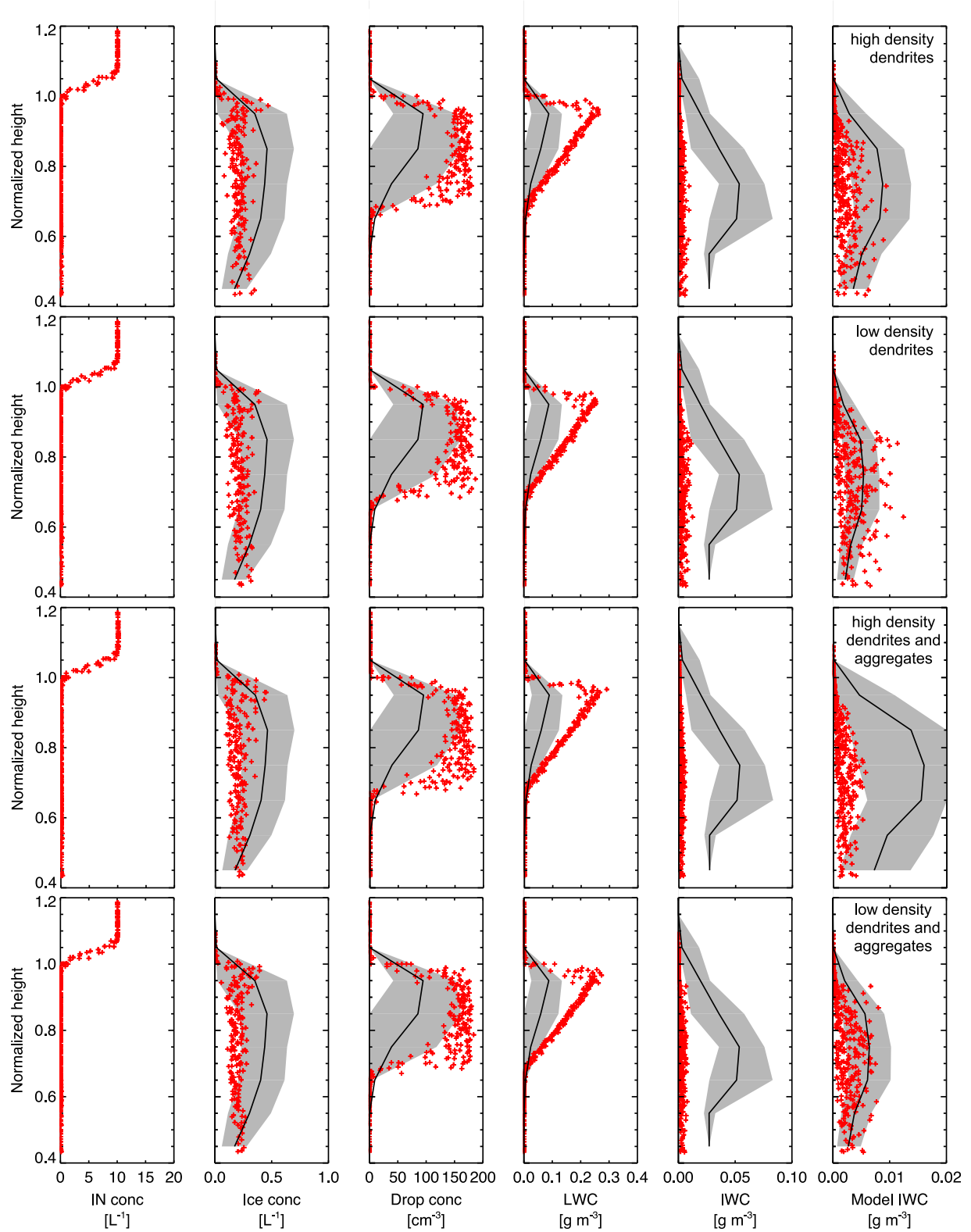


**Figure 10.** Vertical profiles of simulated (red symbols) and horizontally averaged observed (solid line) (left to right) IN concentration, ice number concentration ( $D > 100 \mu\text{m}$ ), droplet number concentration, liquid water content (LWC) and habit-independent and habit-dependent ice water content (denoted in the figures as “IWC” and “Model IWC”) in simulations (first and second rows) with dendrites only and (third and fourth rows) with aggregates and dendrites. Simulated quantities are sampled from the last three hours of the simulations. All simulations use initial IN concentrations of  $10 \text{ L}^{-1}$  above and  $1 \text{ L}^{-1}$  within the boundary layer. Shading denotes 15th–85th-percentile range of observations.

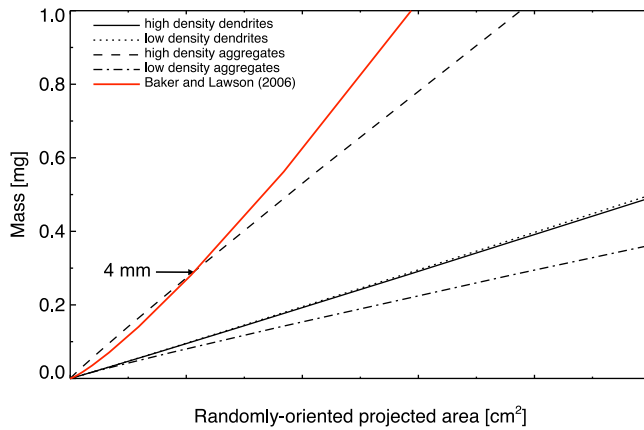


**Figure 11.** Mass-area relations for the ice particles used in the model simulations and for computing IWC. The relationship for high density aggregates provides a good match with the *Baker and Lawson* [2006] relation for particles with maximum dimension of up to 4 mm, but diverges at larger sizes.

continuously increase with height above cloud base until near the cloud top; however, the observed droplet concentrations for individual profiles increase rapidly at cloud base and are then roughly constant throughout the cloud depth before decreasing near cloud top, similar to the simulated fields. Furthermore, the concentration of aerosol particles measured with a PCASP-100X probe over a dry diameter range of  $0.12\text{--}3\text{ }\mu\text{m}$  (not shown) below cloud base during the porpoising leg indicates marked spatial variability that is not captured in the model initialization, increasing from west to east in a manner similar to the drop concentrations (Figure 2). In fact, droplet concentrations, where they are approximately constant with height within the profiles, are comparable to the local aerosol number concentrations below cloud base, consistent with the observations of *Earle et al.* [2011], who conducted aerosol-cloud droplet closure analysis for a similar ISDAC cloud case on April 26 and concluded that a major fraction of the accumulation mode aerosol ( $\sim 90\%$ ) was activated into cloud droplets. The assumed aerosol composition of ammonium bisulfate may also play a secondary role, as composition measurements during other flights indicated that the aerosol mass was dominated by organics and mixtures of organics with sulfates [*McFarquhar et al.*, 2011], which are less hygroscopic, and hence, less effective CCN.

[36] Although simulated ice concentrations show reasonable agreement with observations when measurement uncertainty is taken into account, the IWC in both simulations is about an order of magnitude smaller than the habit-independent IWC estimate. One cause for this discrepancy is illustrated in Figure 11, which presents a comparison of the mass-area relations used in the model simulations with that of *Baker and Lawson* [2006], which was used to infer the IWC from the ice particle size distributions. To calculate the average randomly oriented area of the ice crystals used in the simulations, which is needed for a proper comparison with the *Baker and Lawson* [2006] relation, we took the average randomly oriented projected area of an effectively 2D particle to be one half of its maximum projected area [cf. *Schmitt and Heymsfield*, 2005]. The comparison presented

in Figure 11 reveals that the *Baker and Lawson* [2006] relation implies much denser particles than ordinary dendrites. Only the high density aggregates, which are actually “aggregates of thin plates” [*Mitchell and Heymsfield*, 2005], with a maximum dimension less than about 4 mm, are seen to match the *Baker and Lawson* [2006] relation; for sizes greater than 4 mm a higher density habit is needed. However, the observations show a predominance of dendrites and aggregates of dendrites at all levels (Figure 3). We note that a small amount of ice particles with irregular shapes, which might account for some of the difference, was also present, but our model formulation limits us to representing only the dominant ice crystal habits in the simulations. Indeed, as noted earlier, the model can include any number of ice categories or shapes; however, the uncertainties associated with assigning an ice particle to a certain category and converting particles from one category to another in practice limit the model setup to a small number of ice categories. This inability to reflect the natural variety of ice crystal shapes is not particular to our model but is a limitation of most current models. In Figure 10 we present another IWC estimate computed from the measured ice size distributions and the mass-dimensional relation used in each particular simulation, which we refer to as the habit-dependent IWC. This estimate yields IWC values that are substantially reduced. Intuitively, the application of this estimate seems more appropriate when different model simulations are compared to each other. The simulated IWC shows better agreement with these reduced values.

[37] Figure 12 compares simulated ice size distributions with two estimates of the observed ice size distributions. These estimates are derived from different combinations of instruments (2D-S and 2D-P in the first, shown in green, and 2D-C and 2D-P in the second, shown in black) using different processing algorithms. The differences at sizes smaller than about 0.4 mm are attributable to the different instruments used at these size ranges (2D-S versus 2D-C) and to differences in how the maximum particle dimension is defined in the data processing algorithms. We interpret the differences as an indication of the limits of the accuracy of the measurements. The ice number concentrations and IWC estimates throughout this section are calculated using the distributions derived from the 2D-S and the 2D-P probes. It is seen in Figure 12 that in the simulation with high density dendrites the ice number concentrations are underestimated at all sizes and elevations except below the cloud at sizes around 1 mm. In contrast, simulations with low density dendrites show remarkable agreement with observations at sizes larger than 1–2 mm both below and within the cloud layer. Both simulations considerably underestimate ice concentrations at small sizes below cloud base.

[38] The differences in simulated distributions are reflected in Figure 13 where simulated reflectivities and mean Doppler velocities are compared to those measured by the MMCR and NAWX radars. Simulated reflectivities in the low density simulation with dendrites are about 8–10 dBZ lower than MMCR and NAWX measurements, and in the simulation with high density dendrites the simulated reflectivities are further underestimated by another 2 dBZ. Figure 13 also includes reflectivities computed from measured ice size distributions using the mass-dimensional relation used in each simulation. It is seen in Figure 13 that low density

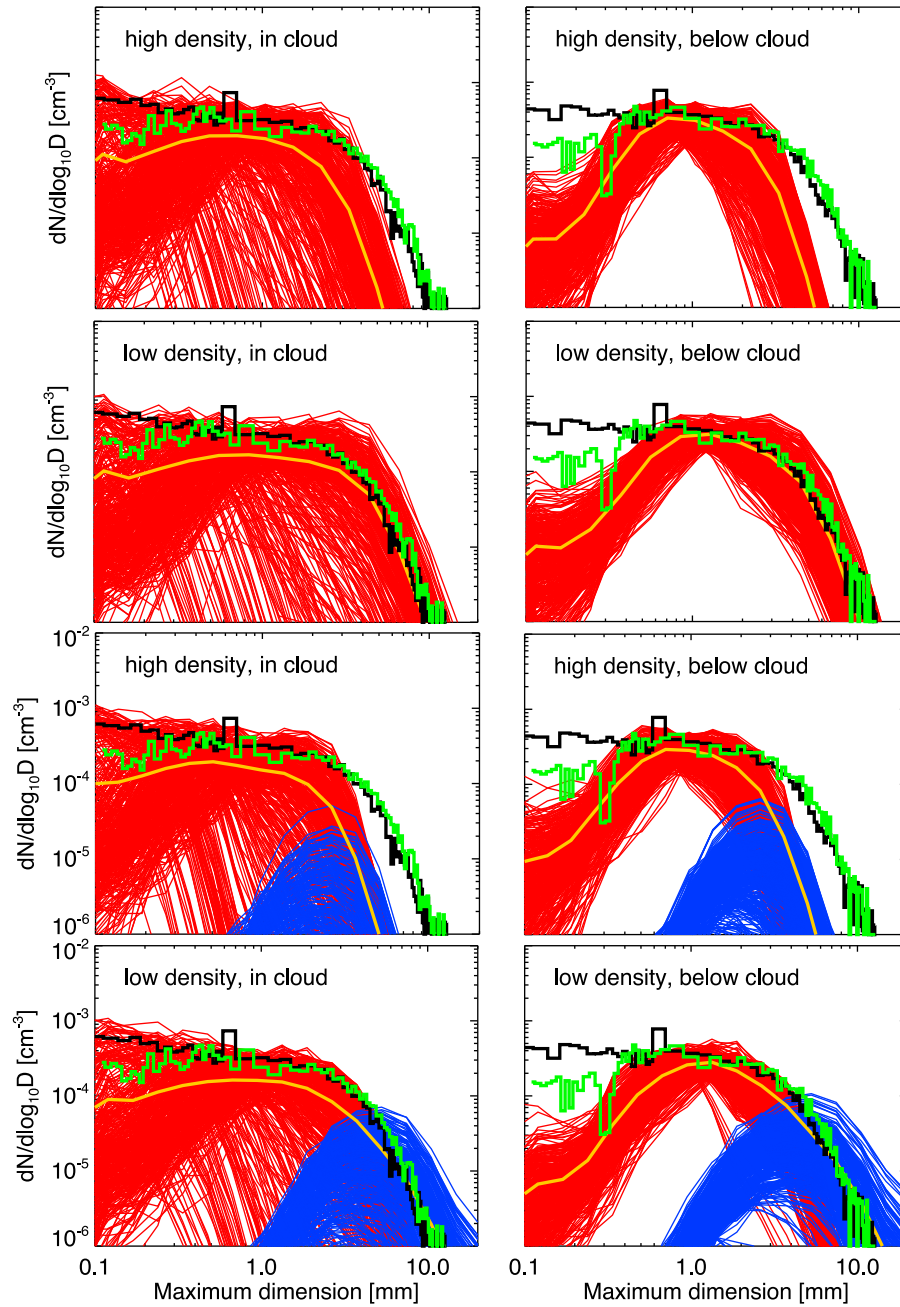


**Figure 12.** Simulated average (yellow solid line) and observed average ice particle number size distributions. Simulated quantities are sampled from the last three hours of the simulations. (first and second rows) Simulation results assuming pristine dendrites with high and low density, respectively. (third and fourth rows) Results from simulations with high and low density dendrites and aggregates. Cloud base height is determined using a threshold value of cloud droplet concentration equal to  $5 \text{ cm}^{-3}$ . The distributions derived from 2D-S and 2D-P probes are shown with green solid line and those from 2D-C and 2D-P probes with black solid line. Individual simulated distributions shown separately for dendrites (red lines) and aggregates (blue lines).

dendrites result in reflectivities about 4 dBZ lower than observed and high density dendrites provide a very good match to both MMCR and NAWX reflectivities. Figure 13 also includes ice fall speeds weighted by simulated reflectivity. Comparison with Figure 6 reveals that they are almost two times slower than those retrieved. However, simulated mean Doppler velocities in both simulations are in

good agreement with those measured by the MMCR, suggesting that the distribution of the simulated mean Doppler velocities is largely determined by the resolved-scale vertical wind variance. Indeed, each model-derived spectrum is much narrower than the observed spectra, with respective widths of 0.1 and  $0.2 \text{ m s}^{-1}$ . The small mean fall speed makes it very difficult to discern any difference between



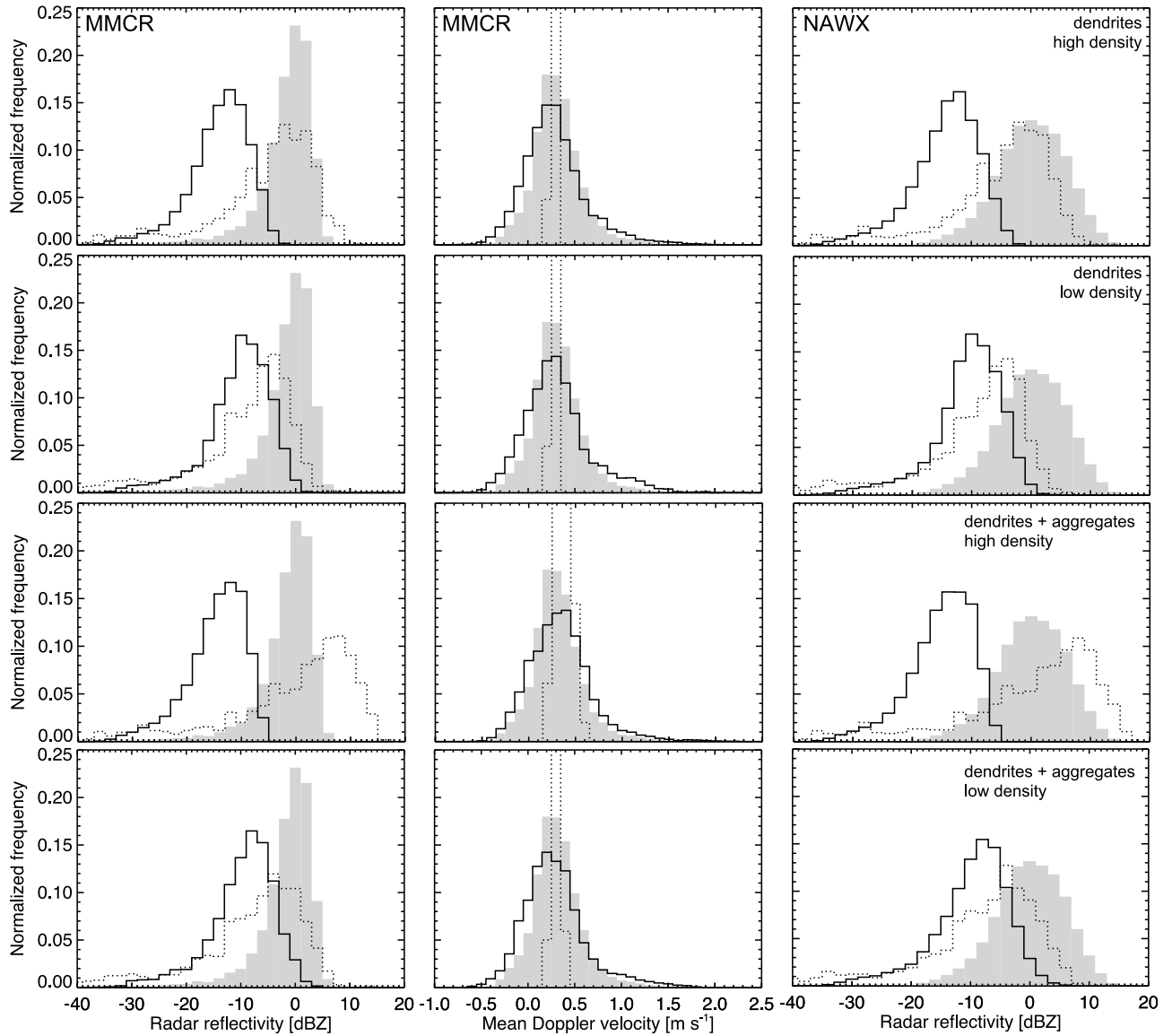


**Figure 13.** Frequency histograms of simulated (black solid line) and observed (shaded) (left) MMCR Ka-band equivalent reflectivities, (middle) mean Doppler velocities and (right) NAWX X-band equivalent reflectivities from below cloud top. Simulated quantities are sampled from the last three hours of the simulations. (first and second rows) Simulation results assuming pristine dendrites with high and low density, respectively. (third and fourth rows) Results from simulations with high and low density dendrites and aggregates. Ice fall speeds (relative to air) shown with dotted line in center panels. Equivalent radar reflectivities calculated from measured ice size distributions shown with dotted line in left and right panels.

simulated and retrieved fall speeds because the retrieved fall speed distribution is so broad (Figure 6). The retrieval method does tend to overestimate fall speeds, with the overall effect of broadening the distribution and producing a mode at large fall speeds.

## 5.2. Simulations With Dendrites and Aggregates

[39] Although the preceding simulations in many ways compare somewhat favorably with the observations, particularly the simulations with low density dendrites, the results are problematic. With very few exceptions, in reality individual dendrites do not grow larger than about 5 mm.

The observed ice size distributions, however, show significant concentrations at larger sizes. Particles with sizes larger than about 5 mm should be aggregates, as indicated by the measurements discussed in Section 2. Aggregation should affect the simulations in two ways: first, it reduces the ice number concentrations directly because two or more ice crystals form one aggregate; and second, aggregates typically fall faster than pristine ice crystals (see Figure 7), thus indirectly reducing ice number concentrations further by increasing the sedimentation loss at the surface.

[40] Simulations with aggregates nonetheless behave in a similar manner to the simulations with dendrites only. Since

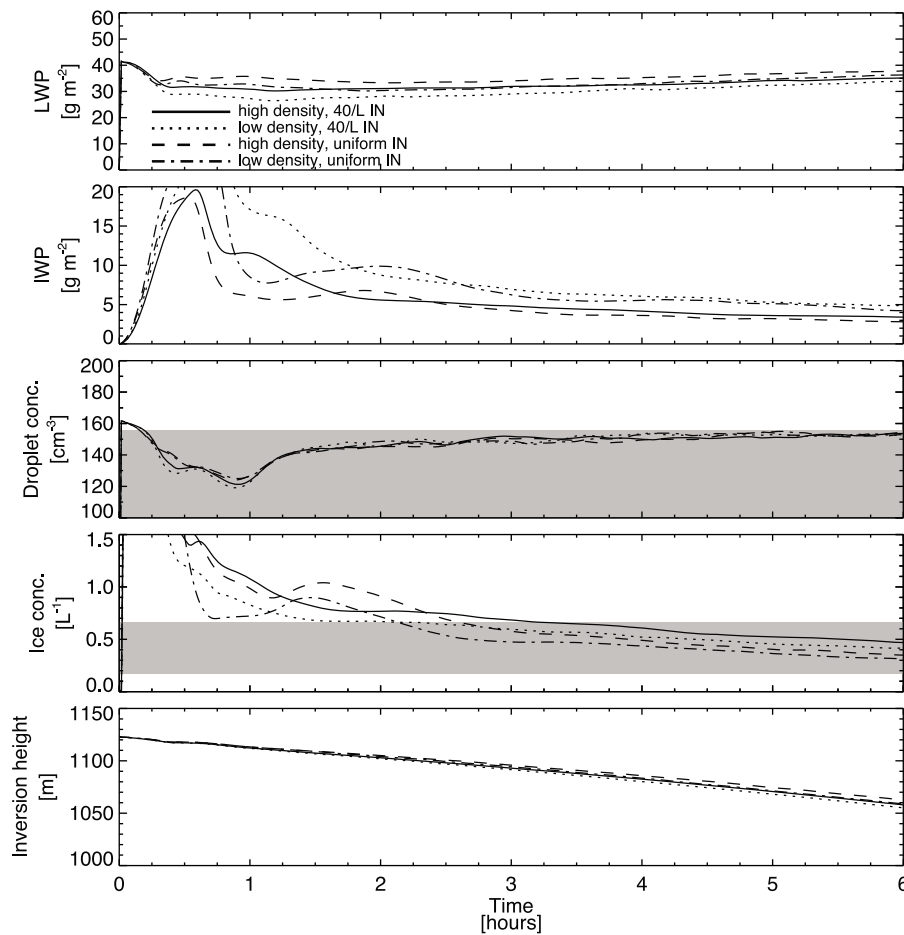


**Figure 14.** Same as Figure 9 but for simulations with both dendrites and aggregates and increased IN concentration or a uniform initial IN profile (see legend).

aggregates have lower depositional growth rates and faster fall speeds compared to individual dendrites, we could expect an increase in the ratio of liquid to ice mass. Indeed, LWP is slightly greater and IWP is reduced compared to the runs with dendrites (Figure 9). Ice number concentrations are also reduced and steadily decrease toward the end of the simulations. As seen in Figure 10, ice number concentrations are commonly underestimated within the cloud layer as in simulations without aggregates. Relative to the simulations with only dendrites, including aggregates leads to a further reduction of ice number concentrations below the cloud, where the aggregation process is most active. IWC is also about an order of magnitude smaller than the habit-independent IWC estimate. In computing habit-dependent IWC, which applies the model's mass-dimensional relations to the observed ice size distributions, we assume that the fraction of dendrites smaller than 2 mm is 100% and it linearly decreases with size until 5 mm, beyond which the fraction of aggregates is 100%, based on a rough estimate using the 2D-P and 2D-C images. The IWC in the high density simulation is about four times smaller than the habit-dependent IWC estimate, while in the low density simulation the agreement is better. As seen in Figure 12, including aggregates results in ice size distributions quite similar to those in simulations with dendrites only, with the most notable difference being increased ice concentrations at the

largest sizes in the simulations with low density ice. As seen in Figure 13, the partitioning of the observed size distributions into dendrites and aggregates, together with mass-dimensional relations assumed in the simulations, results in reflectivities slightly lower (in the low density simulation) and higher (in the high density simulation) than MMCR and NAWX measured reflectivities. Reflectivities based on the model simulations, however, are underestimated in both simulations. This underestimation is a direct consequence of underestimated ice concentrations in these two simulations.

### 5.3. Increased IN Concentrations

[41] Beyond our primary goal of evaluating whether or not the observed IN concentrations are capable of accounting for measured ice concentrations in our modeling framework, we also present simulations with increased IN to address uncertainties in IN measurements and to assess sensitivity to increased IN concentrations. In these simulations we increase the initial IN concentration above the inversion to  $40 \text{ L}^{-1}$ . Below the inversion the initial IN concentration is  $1 \text{ L}^{-1}$ , as before.

[42] As seen in Figure 14, a greater IN concentration leads to a significant increase of IWP and a corresponding reduction in LWP. Ice number concentrations are also increased, and similar to the previous simulations they show a steady decline with a similar decay rate. Quadrupling IN concentrations

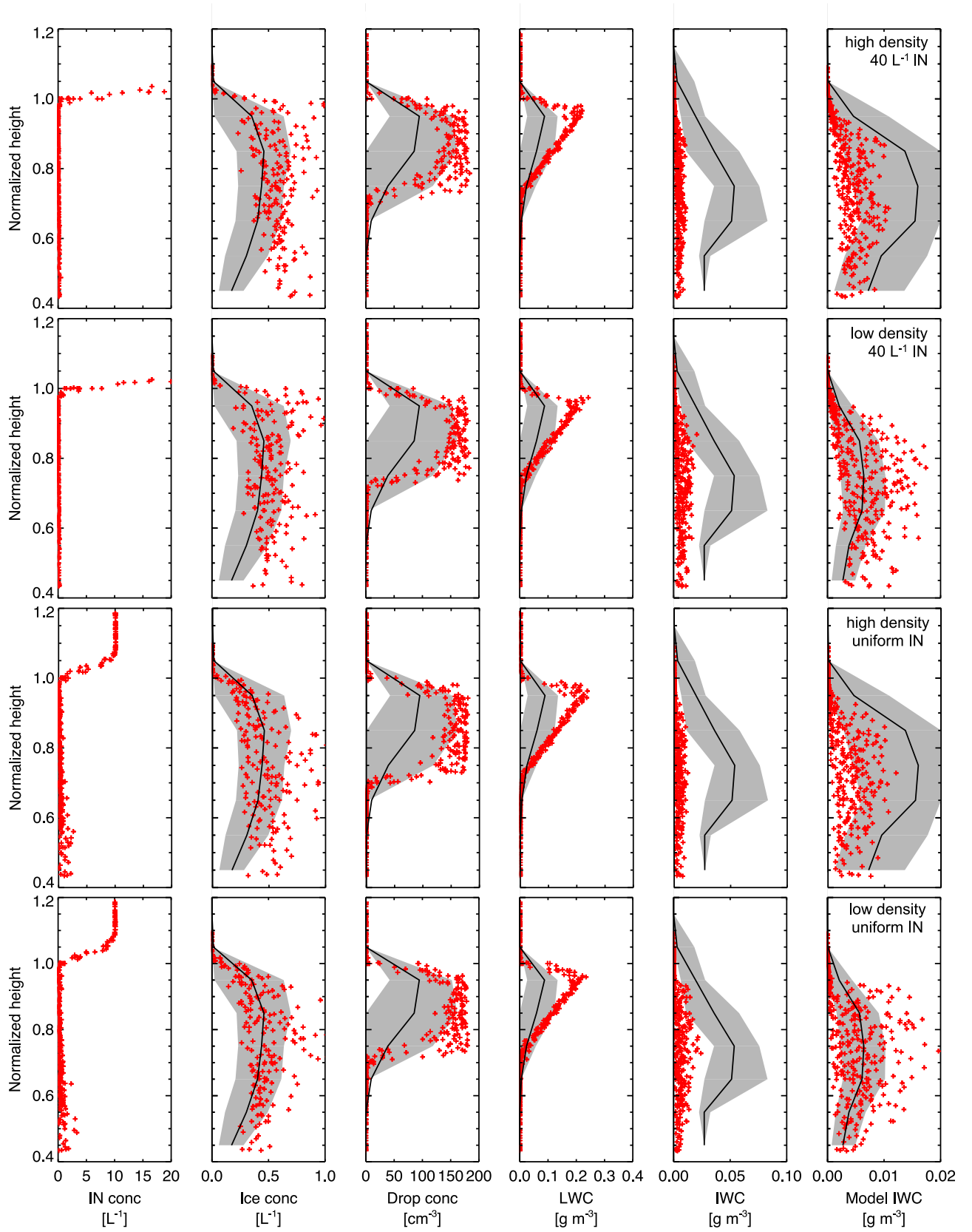


**Figure 15.** Same as Figure 10 but for simulations with high density and low density dendrites and aggregates and (first and second rows) increased IN concentration or (third and fourth rows) a uniform initial IN profile.

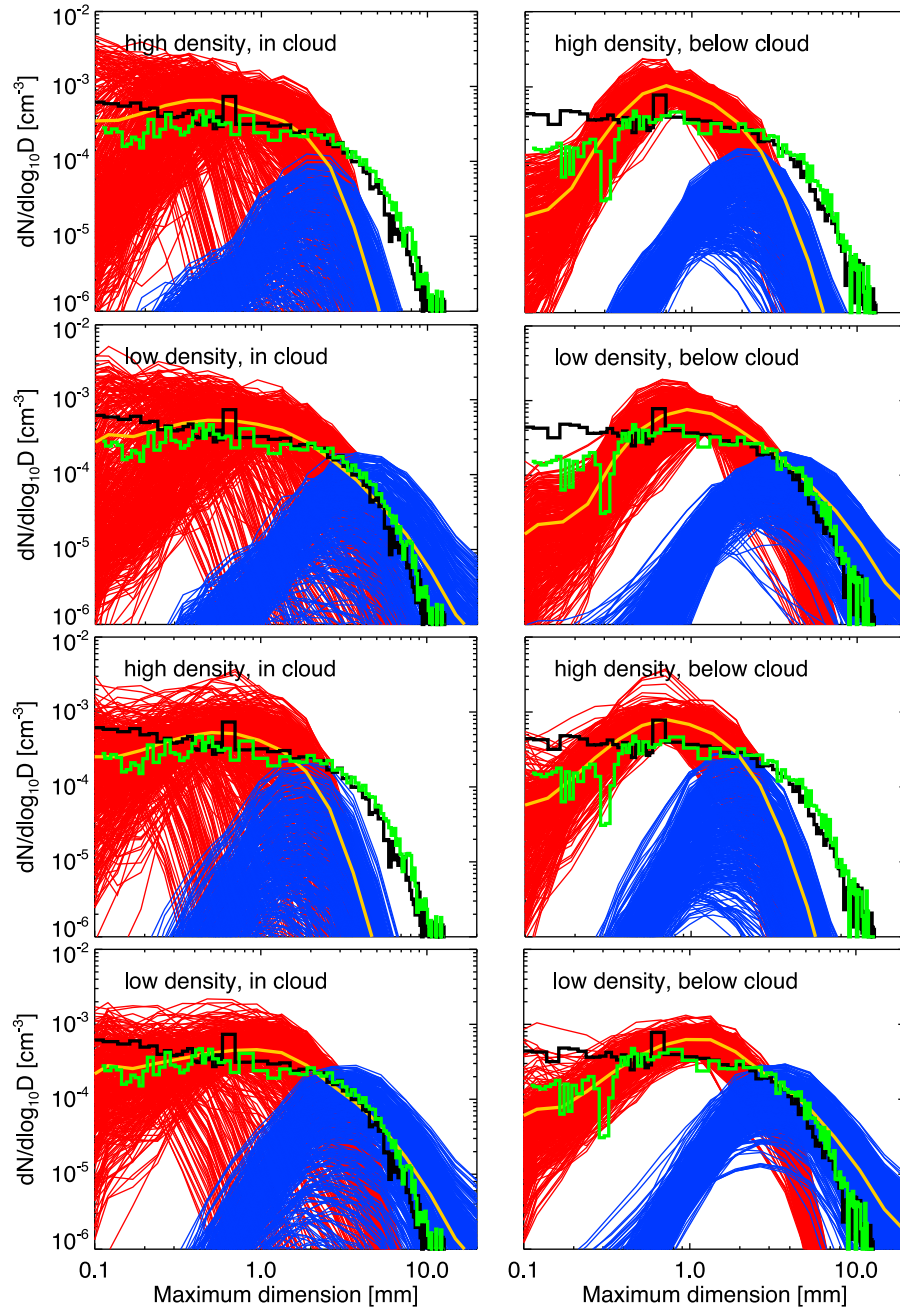


**Figure 16.** Same as Figure 12 but for simulations that involve both dendrites and aggregates, with (first and second rows) increased IN concentration or (third and fourth rows) a uniform initial IN profile.

leads to roughly a doubling of ice number concentrations and IWP, and a one-third reduction of LWP. We note that the differences in LWP and IWP between high density and low density simulations increase with IN concentrations.

[43] The vertical profiles of LWC and IWC show better agreement with observations, although LWC is still overestimated and habit-independent IWC is underestimated (Figure 15). Ice number concentrations are now commonly overestimated below cloud base and again show little variation with height. As seen in Figure 16, ice number concentrations are overestimated at sizes greater than about 0.5 mm in the simulation with low density ice and at intermediate sizes with high density ice. Quadrupling the IN

concentrations brings simulated reflectivities using low density ice into rather good agreement with observations; in the high density ice simulation, however, reflectivities are still underestimated (Figure 17).

#### 5.4. Uniform Initial IN Profile

[44] In the simulations presented thus far we set the initial IN concentration below the inversion roughly equal to the measured ice number concentrations. In the next set of simulations we set the initial IN concentration to  $10 \text{ L}^{-1}$  throughout the domain.

[45] The time series seen in Figure 14 are very similar to those with increased IN aloft. The average ice number

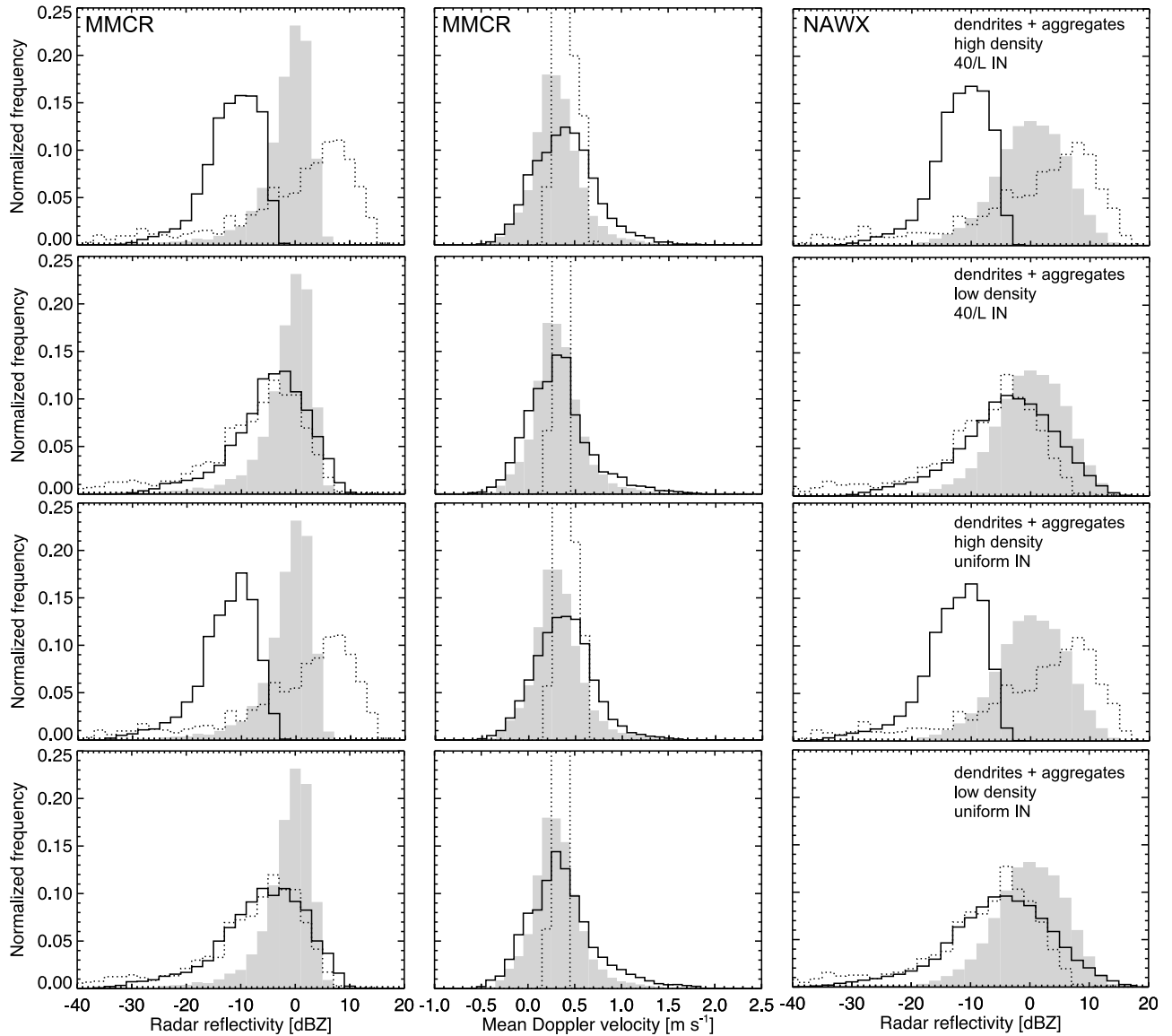


**Figure 17.** Same as Figure 13 but for simulations that involve both dendrites and aggregates, with (first and second rows) increased IN concentration or (third and fourth rows) a uniform initial IN profile.

concentrations do decrease slower than in those other simulations, though, and are about  $0.3 \text{ L}^{-1}$  after six hours of simulation.

[46] In contrast to all of the previous simulations, the boundary layer is not entirely depleted of IN after the first three hours of the simulations (Figure 15). Again, similar to the runs with increased IN aloft, the average ice number concentrations are commonly overestimated in the lower half of the cloud layer and below but the degree of overestimation is reduced in the low density run. In the upper half of the cloud layer the concentrations are similar to the results with observed IN aloft. The average IWC in the simulation with low density ice shows slightly better agreement with observations, but generally the differences in the vertical profiles of the simulated quantities from changes in ice density are not large. As seen in Figure 16 and in contrast to all the other simulations, there is quite good agreement with observed number concentrations of

small ice (with sizes less than 0.5 mm or so) below the cloud layer. At sizes larger than about 2 mm the ice number concentrations are underestimated in the simulation with high density ice. With low density ice, simulated size distributions agree remarkably well with the observations. Simulated radar reflectivities and mean Doppler velocities show quite a good match in the simulation with low density ice (Figure 17). With high density ice in the simulations, the reflectivity is underestimated by about 10 dBZ even though the transition from pristine dendrites to aggregates occurs at smaller sizes than estimated from the observations (Figure 18). Examination of ice particle mass size distributions provides additional insight on this result. As seen in Figure 19, most of the ice mass in the high density simulation is in pristine dendrites rather than aggregates, in contrast to the average mass distribution derived from the observed number distributions and mass-dimensional relations used in the simulations. In the simulation with low

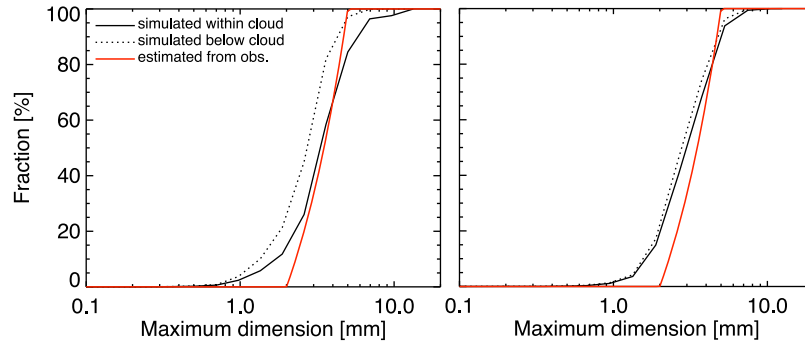


**Figure 18.** Aggregate fraction in simulations with (left) high and (right) low density dendrites and aggregates and a uniform initial IN profile.

density ice, however, most of the ice mass is in the aggregates (Figure 19). There are two reasons for this difference: (1) high density aggregates have significantly greater fall speeds than their low density counterparts (Figure 7), and (2) the aggregation process is less efficient in the high density simulation because of the smaller sizes of the high density ice particles.

[47] An explanation for the dependence of the simulations on the shape of the initial IN profile is illustrated in Figure 20, which shows the evolution of vertical wind variance (a measure of the intensity of convective mixing) and IN concentration. The cloud layer forms below the inversion and through convection driven by cloud top radiative cooling deepens the mixed layer. Because most of the

boundary layer is under-saturated with respect to ice, IN are not activated below the cloud base, leaving a reservoir of IN between the cloud layer and the surface. As the mixed-layer deepens, it slowly mixes IN into the cloud layer where they can be activated. Thus, entrainment from below helps to maintain relatively constant ice concentrations until the IN would ultimately be depleted, were the mixed-layer to eventually reach the surface. This mechanism is also operational, albeit with weaker effect, in the simulations where the initial IN concentrations under the inversion were set to  $1 \text{ L}^{-1}$  (Figure 20). The relative importance of the two entrainment mechanisms can be evaluated through comparison with the respective IN fluxes into the well-mixed cloud layer. The entrainment rate of overlying air is roughly

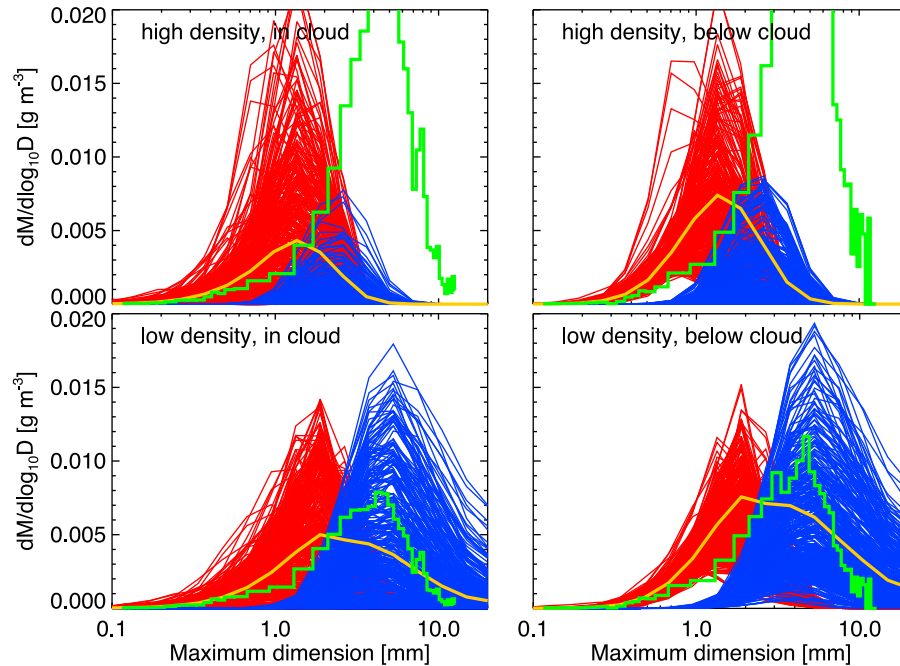


**Figure 19.** Ice particle mass distributions from simulations and derived from measurements. Simulated quantities are sampled from the last three hours of the simulations. Simulations and derivations using dendrites and aggregates of (top) high and (bottom) low density and a uniform initial IN profile are shown. Distributions derived from 2D-S and 2D-P probes using the mass-dimensional relation used in the corresponding simulations are shown with green line. Individual distributions sampled from the model simulations are shown separately for dendrites (red lines) and aggregates (blue lines) and the combined average shown with yellow lines.



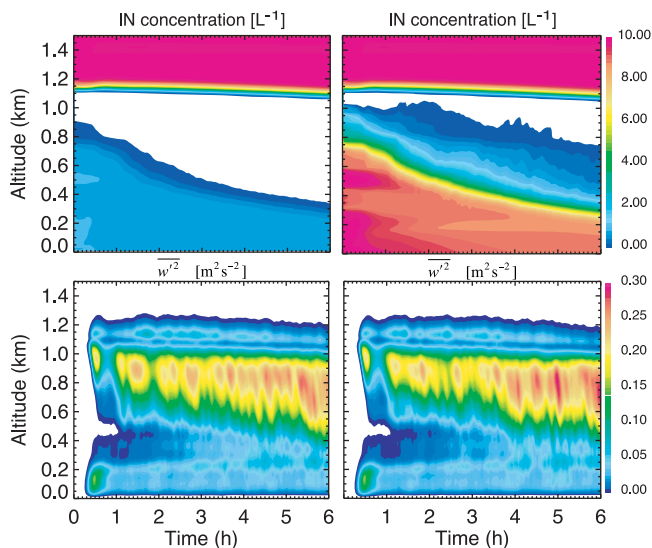


**Figure 20.** (top) IN concentration and (bottom) vertical velocity variance for simulations that include low density dendrites and aggregates; (left) with initial IN concentrations of  $10 \text{ L}^{-1}$  above and  $1 \text{ L}^{-1}$  within the boundary layer and (right) with a vertically uniform IN concentration of  $10 \text{ L}^{-1}$ .

$1 \text{ cm s}^{-1}$  over the last 3 h of the simulation, and the entrainment rate of underlying air is about 50% faster. Thus, for an initial IN concentration of  $10 \text{ L}^{-1}$  in the boundary layer, the IN source from below is about 50% greater than that from above, and for an initial concentration in the boundary layer one tenth of the overlying value, the IN source from above is about seven times greater than that from below. It is the source from below that leads to an increase in concentrations of small ice when assuming a uniform initial IN profile.

### 5.5. Further Sensitivity Tests

[48] We made a number of choices in the simulation setup on assumptions that deserve inspection. To assess the impact of these choices on our results, we ran additional simulations where these choices were reversed. We will only summarize the results of these simulations without describing them in detail.

[49] One choice is the assumption that IN could be activated by any of the classical nucleation mechanisms even though the CFDC may undercount IN active in the contact mode. To evaluate this choice, we ran a simulation in which only condensation and deposition freezing were allowed. No discernible difference was found between these two runs, so we find that including contact nucleation and immersion freezing did not affect our results.

[50] Another choice was to neglect IN recycling from complete sublimation. Thus, we ran a simulation in which such IN recycling was included, and it also did not result in any discernible difference, despite the fact that a substantial portion of the boundary layer is under-saturated with respect to ice in the simulations. We attribute the lack of an impact from IN recycling to the low concentrations of ice small enough to completely sublimate under the cloud. A shallow layer, about 100-m thick, near the surface with enhanced IN

concentrations did develop in response to IN recycling. Although evidently insufficient numbers of IN from this layer were mixed into the cloud layer to alter the ice population in the course of the 6-h long simulation, it is possible that IN recycling could be instrumental in maintaining ice concentrations on longer time scales.

[51] We also carried out a sensitivity test designed to assess the impact of the aspect ratio assumed for aggregates. A recent modeling study [Hashino and Tripoli, 2011a, 2011b] found that the aspect ratio of aggregates composed of dendrites increases up to 0.33 as the number of component crystals builds to ten and remains constant as more component crystals are added. In light of this result, we assumed an aspect ratio for aggregates of 0.35 (compare to 0.1 in our other simulations) and found no discernible differences in the results.

[52] As noted in Section 4, the large-scale subsidence imposed in our simulations is likely overestimated. For a sensitivity test we used a subsidence rate that at the initial height of the inversion is  $0.5 \text{ cm s}^{-1}$ , derived from the ECMWF reanalysis, which is less than half the subsidence rate of  $1.1 \text{ cm s}^{-1}$  that we used in our other simulations. As could be expected from reducing the subsidence rate, the boundary layer gradually deepened through the course of the simulation, resulting in less than a 10% reduction in the entrainment rate. No significant differences in other simulation diagnostics, particularly ice number concentrations, were evident (not shown). The simulated entrainment rate is evidently resistant to changes in subsidence rate, as the deepening of the boundary layer largely compensates for the imposed reduction in subsidence. Such resistance is consistent with the entrainment rate being predominantly set by the strength of boundary layer convection, which is primarily determined by cloud top radiative cooling in stratocumulus [e.g., Stevens *et al.*, 2005], though microphysical processes also play a role [e.g., Stevens *et al.*, 1998; Bretherton *et al.*, 2007; Ackerman *et al.*, 2009].

[53] Finally, a run with the final version of the aerosol data showed that the only field affected was the average droplet concentration, which increased less than 10%.

## 6. Discussion and Summary

[54] We have presented results from large-eddy simulations of a low-lying mixed-phase cloud layer observed during ISDAC. Our intent in conducting these simulations was to test the hypothesis that the IN concentrations measured above the cloud layer can explain the observed concentrations of ice with maximum dimension  $>100 \mu\text{m}$  while satisfying other observational constraints for this case study. Under the environmental conditions of this case it is expected that ice concentrations should be determined by several factors: the concentration of IN above the cloud layer, the rate at which IN are entrained into the cloud layer from above, the fall speed of the ice crystals and the rate of aggregation. The case we have simulated presents the most favorable conditions for such a closure to be achieved: the observed IN concentrations were among the greatest measured in the Arctic, the predominant ice crystal habit is characterized by slow fall speeds and measured ice particle number concentrations were less than the overlying IN concentrations.

[55] We ran a number of simulations to account for uncertainties in IN measurements, as well as ice crystal geometry and habit mixture. To start, we considered only two dendrite types: either broad-armed (high density) or stellar (low density). Simulations with either dendrite type showed reasonable agreement with the observed ice number concentrations and size distributions, but radar reflectivities and ice water content were severely underestimated. Simulated and observed Doppler velocities also showed reasonable agreement, but simulated reflectivity-weighted fall speeds were roughly a factor of two slower than retrieved. Since observations clearly indicated the predominance of aggregates at large sizes, we also conducted simulations with aggregates in addition to dendrites. Including aggregates (assumed to be composed of either high density or low density component crystals, respectively) led to only slightly reduced ice number concentrations under the cloud layer and overall provided a similar match to the observations, including a roughly 10 dBZ underestimate of radar reflectivities. Two simulations with low density dendrites and aggregates were found to provide a better match to radar reflectivities: one in which IN concentrations were increased fourfold (recall that IN measurements were all below water saturation) and a second in which IN concentrations were initialized with a vertically uniform profile. A key aspect of the simulations with vertically uniform IN initial profiles was a reservoir of IN that remained under the well-mixed cloud layer. As the simulations progressed and the well-mixed layer deepened, the reservoir IN slowly mixed upward, helping to maintain ice concentrations close to those observed. We note, however, that we have no independent verification that the dendrites and aggregates were in fact low density. Such quantitative information is not provided by current measurements, leading to the bounding approach used here (high density versus low density). Thus, model parameters were insufficiently constrained.

[56] Given the uncertainties of the measurements and parameterizations of the microphysical processes embedded in the model, on one hand we find that the degree of agreement between simulated and measured ice number concentrations is generally within uncertainty in all these simulations. This agreement contrasts with previous modeling studies of Arctic mixed-phase clouds, which typically show a large discrepancy when the observed IN concentrations above the boundary layer were used — and treated prognostically. The most obvious reasons for the agreement here are the high IN concentrations and the slow ice fall speeds in this case study. A more detailed analysis of the simulations, however, reveals other reasons why this case is different. The ice concentrations in all our simulations gradually decrease with time without reaching a steady state by the end of the six-hour simulations, indicating that the ice concentrations in the simulations are influenced by the entrainment of IN from a reservoir under the cloud layer. Only after the reservoir is largely depleted would the IN entrainment from above become the limiting factor controlling ice concentrations. Such a scenario is quite different from a well-mixed boundary layer, where any IN initially under the cloud layer are rapidly depleted [Harrington and Olsson, 2001; Fridlind *et al.*, 2007].

[57] On the other hand, our results do agree with previous studies that show ice concentrations within the boundary

layer at least an order of magnitude smaller than the overlying IN concentrations [Morrison *et al.*, 2005; Fridlind *et al.*, 2007; Fan *et al.*, 2009; Avramov and Harrington, 2010]. A lower bound of the ratio of IN concentration above the boundary layer to ice crystals within it can be estimated by neglecting the IN source from below, yielding a ratio of about 50 for the low density dendrites alone and greater for all other simulations.

[58] The vast difference between the IN concentration above and the ice concentration within the cloud layer contradicts the argument put forward by Prenni *et al.* [2009] that IN concentrations roughly equal to the observed ice concentrations within a cloud layer should be sufficient to explain the ice formation in Arctic mixed-phase clouds. We note that such parity could be attained in a model simulation only if an effectively unlimited source of IN within the cloud layer were to be assumed (i.e., in simulations with diagnostic treatment of IN with its concentration equal to the overlying value) or an effective sink of IN were neglected (i.e., through ice crystal sedimentation). With a diagnostic treatment of IN, ice concentrations even greater than IN concentrations are possible. Also, while neglecting the sedimentation of ice may be reasonable for the fast transit times of air parcels through wave clouds [e.g., Cotton and Field, 2002; Eidhammer *et al.*, 2010], it is not a reasonable assumption for mixed-phase clouds in the Arctic boundary layer, where air parcels cycle through clouds many times [Shupe *et al.*, 2008a].

[59] Even though ice number concentrations roughly match observations here, other aspects of the simulations fail to agree with the observations. Comparison of observed ice water contents and radar reflectivities with values calculated from simulated and observed size distributions, assuming a range of mass-dimensional relations with and without aggregates, sheds additional light on likely model shortcomings. In particular, assuming the presence of low density dendrites and aggregates provides close agreement between reflectivities observed and calculated from in situ size distributions, but the corresponding ice water content is roughly an order of magnitude lower than the habit-independent estimate. By contrast, high density aggregates evidently sediment too quickly, resulting in underestimated number concentrations at large sizes in the simulations. Although this underestimation has little effect on total ice number concentrations, it results in (habit-dependent) ice mass concentrations that significantly underestimate the habit-independent values inferred from the measurements.

[60] A critical, unconstrained aspect of the simulations is the size-segregated properties of ice, such as the percentage of aggregates and the distribution of their properties as a function of mass or size. Owing to a lack of such constraint, in this study we attempted to bound possible values by using high density and low density ice and found results to be highly sensitive to the assumed properties.

[61] **Acknowledgments.** We thank Steven Ghan (ISDAC project scientist) and the flight crew of the NRC Convair-580 for making these measurements possible. We also thank Peter Liu and Michael Earle of Environment Canada for providing the best-estimate aerosol size distribution for this case. We are grateful to the three anonymous reviewers for helpful comments. This research used resources of the National Energy Research Scientific Computing Center, which is supported by the DOE

Office of Science under contract DE-AC02-05CH11231. This work was supported by the DOE Office of Science, Office of Biological and Environmental Research, through Interagency Agreements DE-AI02-06ER64173 and DE-AI02-08ER64547, and by the NASA Radiation Sciences Program. ARM data are made available through the U.S. Department of Energy as part of the Atmospheric Radiation Measurement Program.

## References

- Ackerman, A. S., O. B. Toon, and P. V. Hobbs (1995), A model for particle microphysics, turbulent mixing, and radiative-transfer in the stratocumulus-topped marine boundary layer and comparisons with measurements, *J. Atmos. Sci.*, **52**(8), 1204–1236, doi:10.1175/1520-0469(1995)052<1204:AMFPMT>2.0.CO;2.
- Ackerman, A. S., M. P. Kirkpatrick, D. E. Stevens, and O. B. Toon (2004), The impact of humidity above stratiform clouds on indirect aerosol climate forcing, *Nature*, **432**(7020), 1014–1017, doi:10.1038/nature03174.
- Ackerman, A. S., et al. (2009), Large-eddy simulations of a drizzling, stratocumulus-topped marine boundary layer, *Mon. Weather Rev.*, **137**, 1083–1110, doi:10.1175/2008MWR2582.1.
- Avramov, A., and J. Y. Harrington (2010), Influence of parameterized ice habit on simulated mixed phase Arctic clouds, *J. Geophys. Res.*, **115**, D03205, doi:10.1029/2009JD012108.
- Baker, B., and R. P. Lawson (2006), Improvement in determination of ice water content from two-dimensional particle imagery. Part I: Image-to-mass relationships, *J. Appl. Meteorol. Climatol.*, **45**, 1282–1290, doi:10.1175/JAM2398.1.
- Beard, K. V., and H. T. Ochs (1984), Collection and coalescence efficiencies for accretion, *J. Geophys. Res.*, **89**(D5), 7165–7169, doi:10.1029/JD089iD05p07165.
- Böhm, H. (1989), A general equation for the terminal fall speed of solid hydrometeors, *J. Atmos. Sci.*, **46**, 2419–2427, doi:10.1175/1520-0469(1989)046<2419:AGEFTT>2.0.CO;2.
- Böhm, J. P. (1992a), A general hydrodynamic theory for mixed-phase microphysics. Part I: Drag and fall speed of hydrometeors, *Atmos. Res.*, **27**(4), 253–274, doi:10.1016/0169-8095(92)90035-9.
- Böhm, J. P. (1992b), A general hydrodynamic theory for mixed-phase microphysics. Part II: Collision kernels for coalescence, *Atmos. Res.*, **27**(4), 275–290, doi:10.1016/0169-8095(92)90036-A.
- Böhm, J. P. (1992c), A general hydrodynamic theory for mixed-phase microphysics. Part III: Riming and aggregation, *Atmos. Res.*, **28**(2), 103–123, doi:10.1016/0169-8095(92)90023-4.
- Böhm, J. P. (1994), Theoretical collision efficiencies for riming and aerosol impaction, *Atmos. Res.*, **32**(1–4), 171–187, doi:10.1016/0169-8095(94)90058-2.
- Böhm, J. P. (1999), Revision and clarification of “A general hydrodynamic theory for mixed-phase microphysics,” *Atmos. Res.*, **52**(3), 167–176, doi:10.1016/S0169-8095(99)00033-2.
- Böhm, J. P. (2004), Reply to comment on “Revision and clarification of ‘A general hydrodynamic theory for mixed-phase microphysics’ [Böhm J.P., 1999, *Atmos. Res.* **52**, 167–176],” *Atmos. Res.*, **69**(3–4), 289–293, doi:10.1016/j.atmosres.2003.10.001.
- Botta, G., K. Aydin, and J. Verlinde (2010), Modeling of microwave scattering from cloud ice crystal aggregates and melting aggregates: A new approach, *IEEE Geosci. Remote Sens. Lett.*, **7**(3), 572–576, doi:10.1109/LGRS.2010.2041633.
- Botta, G., K. Aydin, J. Verlinde, A. Avramov, A. Ackerman, A. Fridlind, M. Wolde, and G. McFarquhar (2011), Millimeter wave scattering from ice crystals and their aggregates: Comparing cloud model simulations with X- and Ka-band radar measurements, *J. Geophys. Res.*, **116**, D00T04, doi:10.1029/2011JD015909.
- Bretherton, C. S., P. N. Blossey, and J. Uchida (2007), Cloud droplet sedimentation, entrainment efficiency, and subtropical stratocumulus albedo, *Geophys. Res. Lett.*, **34**, L03813, doi:10.1029/2006GL027648.
- Businger, J. A., J. C. Wyngaard, Y. Izumi, and E. F. Bradley (1971), Flux-profile relationships in the atmospheric surface layer, *J. Atmos. Sci.*, **28**, 181–189, doi:10.1175/1520-0469(1971)028<0181:FPRITA>2.0.CO;2.
- Cantrell, W., and A. Heymsfield (2005), Production of ice in tropospheric clouds: A review, *Bull. Am. Meteorol. Soc.*, **86**, 795–807, doi:10.1175/BAMS-86-6-795.
- Clothiaux, E. E., T. P. Ackerman, G. G. Mace, K. P. Moran, R. T. Marchand, M. Miller, and B. E. Martner (2000), Objective determination of cloud heights and radar reflectivities using a combination of active remote sensors at the ARM CART sites, *J. Appl. Meteorol.*, **39**, 645–665, doi:10.1175/1520-0450(2000)039<0645:ODOCHA>2.0.CO;2.
- Cotton, R. J., and P. R. Field (2002), Ice nucleation characteristics of an isolated wave cloud, *Q. J. R. Meteorol. Soc.*, **128**, 2417–2437, doi:10.1256/qj.01.150.
- Curry, J. A., W. B. Rossow, D. Randall, and J. L. Schramm (1996), Overview of Arctic cloud and radiation characteristics, *J. Clim.*, **9**, 1731–1764, doi:10.1175/1520-0442(1996)009<1731:OOACAR>2.0.CO;2.
- de Boer, G., T. Hashino, and G. J. Tripoli (2010), Ice nucleation through immersion freezing in mixed-phase stratiform clouds: Theory and numerical simulations, *Atmos. Res.*, **96**(2–3), 315–324, doi:10.1016/j.atmosres.2009.09.012.
- Earle, M. E., P. S. K. Liu, J. W. Strapp, A. Zelenyuk, D. G. Imre, G. M. McFarquhar, N. C. Shantz, and R. Leaitch (2011), Factors influencing the microphysics and radiative properties of liquid-dominated Arctic clouds: insight from observations of aerosol and clouds during ISDAC, *J. Geophys. Res.*, doi:10.1029/2011JD015887, in press.
- Eidhammer, T., et al. (2010), Ice initiation by aerosol particles: Measured and predicted ice nuclei concentrations versus measured ice crystal concentration in an orographic wave cloud, *J. Atmos. Sci.*, **67**, 2417–2436, doi:10.1175/2010JAS3266.1.
- Fan, J., M. Ovtchinnikov, J. M. Comstock, S. A. McFarlane, and A. Khain (2009), Ice formation in Arctic mixed-phase clouds: Insights from a 3-D cloud-resolving model with size-resolved aerosol and cloud microphysics, *J. Geophys. Res.*, **114**, D04205, doi:10.1029/2008JD010782.
- Field, P. R., A. J. Heymsfield, and A. Bansemer (2006), Shattering and particle interarrival times measured by optical array probes in ice clouds, *J. Atmos. Oceanic Technol.*, **23**, 1357–1371, doi:10.1175/JTECH1922.1.
- Fornea, A. P., S. D. Brooks, J. B. Dooley, and A. Saha (2009), Heterogeneous freezing of ice on atmospheric aerosols containing ash, soot, and soil, *J. Geophys. Res.*, **114**, D13201, doi:10.1029/2009JD011958.
- Fridlind, A. M., A. S. Ackerman, G. McFarquhar, G. Zhang, M. R. Poellot, P. J. DeMott, A. J. Prenni, and A. J. Heymsfield (2007), Ice properties of single-layer stratocumulus during the Mixed-Phase Arctic Cloud Experiment: 2. Model results, *J. Geophys. Res.*, **112**, D24202, doi:10.1029/2007JD008646.
- Fridlind, A. M., B. van Diedenhoven, A. S. Ackerman, A. Avramov, A. Mrowiec, H. Morrison, P. Zuidema, and M. D. Shupe (2011), A FIRE-ACE/SHEBA case study of mixed-phase Arctic boundary-layer clouds: Entrainment rate limitations on rapid primary ice nucleation processes, *J. Atmos. Sci.*, doi:10.1175/JAS-D-11-052.1, in press.
- Gultepe, I., G. Isaac, D. Hudak, R. Nissen, and J. W. Strapp (2000), Dynamical and microphysical characteristics of Arctic clouds during BASE, *J. Clim.*, **13**, 1225–1254, doi:10.1175/1520-0442(2000)013<1225:DAMCOA>2.0.CO;2.
- Hallett, J., and S. C. Mossop (1974), Production of secondary ice particles during the riming process, *Nature*, **249**, 26–28, doi:10.1038/249026a0.
- Harrington, J. Y., and P. Q. Olsson (2001), On the potential influence of ice nuclei on surface-forced marine stratocumulus cloud dynamics, *J. Geophys. Res.*, **106**, 27,473–27,484, doi:10.1029/2000JD000236.
- Harrington, J. Y., T. Reislin, W. R. Cotton, and S. M. Kreidenweis (1999), Cloud resolving simulations of Arctic stratus. Part II: Transition-season clouds, *Atmos. Res.*, **51**, 45–75, doi:10.1016/S0169-8095(98)00098-2.
- Hashino, T., and G. J. Tripoli (2011a), The Spectral Ice Habit Prediction System (SHIPS). Part III: Description of the ice particle model and the habit-dependent aggregation model, *J. Atmos. Sci.*, **68**, 1125–1141, doi:10.1175/2011JAS3666.1.
- Hashino, T., and G. J. Tripoli (2011b), The Spectral Ice Habit Prediction System (SHIPS). Part IV: Box model simulations of the habit-dependent aggregation process, *J. Atmos. Sci.*, **68**, 1142–1161, doi:10.1175/2011JAS3667.1, in press.
- Haynes, J. M., Z. Luo, G. L. Stephens, R. T. Marchand, and A. Bodas-Salcedo (2007), A multipurpose radar simulation package: QuickBeam, *Bull. Am. Meteorol. Soc.*, **88**, 1723–1727, doi:10.1175/BAMS-88-11-1723.
- Heymsfield, A. J., and C. D. Westbrook (2010), Advances in the estimation of ice particle fall speeds using laboratory and field measurements, *J. Atmos. Sci.*, **67**, 2469–2482, doi:10.1175/2010JAS3379.1.
- Hobbs, P. V., and A. L. Rangno (1998), Microstructure of low- and middle-level clouds over the Beaufort Sea, *Q. J. R. Meteorol. Soc.*, **124**, 2035–2071, doi:10.1002/qj.49712455012.
- Jiang, H., W. R. Cotton, J. O. Pinto, J. A. Curry, and M. J. Weissbluth (2000), Sensitivity of mixed-phase Arctic stratocumulus to ice forming nuclei and large-scale heat and moisture advection, *J. Atmos. Sci.*, **57**, 2105–2117, doi:10.1175/1520-0469(2000)057<2105:CRSOMP>2.0.CO;2.
- Kajikawa, M. (1989), Observation of the falling motion of early snowflakes. Part II: On the variation of falling velocity, *J. Meteorol. Soc. Jpn.*, **67**, 731–737.
- Kirkpatrick, M. P., A. S. Ackerman, D. E. Stevens, and N. N. Mansour (2006), On the application of the dynamic Smagorinsky model to large-eddy simulations of the cloud-topped atmospheric boundary layer, *J. Atmos. Sci.*, **63**, 526–546, doi:10.1175/JAS3651.1.

- Klein, S. A., et al. (2009), Intercomparison of model simulations of mixed-phase clouds observed during the ARM Mixed-Phase Arctic Cloud Experiment. I: Single-layer cloud, *Q. J. R. Meteorol. Soc.*, **135**, 979–1002, doi:10.1002/qj.416.
- Kollias, P., E. E. Clothiaux, M. A. Miller, E. P. Luke, K. L. Johnson, K. P. Moran, K. B. Widener, and B. A. Albrecht (2007), The Atmospheric Radiation Measurement Program cloud profiling radars: Second-generation sampling strategies, processing, and cloud data products, *J. Atmos. Oceanic Technol.*, **24**, 1199–1214, doi:10.1175/JTECH2033.1.
- Korolev, A., and B. Sussman (2000), A technique for habit classification of cloud particles, *J. Atmos. Oceanic Technol.*, **17**, 1048–1057, doi:10.1175/1520-0426(2000)017<1048:ATFHCO>2.0.CO;2.
- Korolev, A. V., E. F. Emery, J. W. Strapp, S. G. Cober, G. A. Isaac, M. Wasey, and D. Marcotte (2011), Small ice particles in tropospheric clouds: Fact or artifact? Airborne Icing Instrumentation Evaluation Experiment, *Bull. Am. Meteorol. Soc.*, doi:10.1175/2010BAMS3141.1, in press.
- Lawson, R. P. (2011), Effects of ice particles shattering on optical cloud particle probes, *Atmos. Meas. Tech. Discuss.*, **4**, 939–968, doi:10.5194/amtd-4-939-2011.
- Lawson, R. P., and P. Zuidema (2009), Aircraft microphysical and surface-based radar observations of summertime Arctic clouds, *J. Atmos. Sci.*, **66**, 3505–3529, doi:10.1175/2009JAS3177.1.
- List, R., and R. S. Schemenauer (1971), Free-fall behavior of planar snow crystals, conical graupel and small hail, *J. Atmos. Sci.*, **28**, 110–115, doi:10.1175/1520-0469(1971)028<0110:FFBOPS>2.0.CO;2.
- Luo, Y., K.-M. Xu, H. Morrison, and G. McFarquhar (2008), Arctic mixed-phase clouds simulated by a cloud-resolving model: Comparison with ARM observations and sensitivity to microphysics parameterizations, *J. Atmos. Sci.*, **65**, 1285–1303, doi:10.1175/2007JAS2467.1.
- McFarquhar, G. M., G. Zhang, M. R. Poellot, G. L. Kok, R. McCoy, T. Tooman, A. Fridlind, and A. J. Heymsfield (2007), Ice properties of single-layer stratocumulus during the Mixed-Phase Arctic Cloud Experiment: 1. Observations, *J. Geophys. Res.*, **112**, D24201, doi:10.1029/2007JD008633.
- McFarquhar, G. M., et al. (2011), Indirect and Semi-Direct Aerosol Campaign (ISDAC): The impact of Arctic aerosols on clouds, *Bull. Am. Meteorol. Soc.*, **92**, 183–201, doi:10.1175/2010BAMS2935.1.
- Meyers, M. P., P. J. Demott, and W. R. Cotton (1992), New primary ice-nucleation parameterizations in an explicit cloud model, *J. Appl. Meteorol.*, **31**, 708–721, doi:10.1175/1520-0450(1992)031<0708:NPINPI>2.0.CO;2.
- Mitchell, D. L. (1988), Evolution of snow-size spectra in cyclonic storms. Part I: Snow growth by vapor deposition and aggregation, *J. Atmos. Sci.*, **45**, 3431–3451, doi:10.1175/1520-0469(1988)045<3431:EOSSSI>2.0.CO;2.
- Mitchell, D. L. (1996), Use of mass- and area-dimensional power laws for determining precipitation particle terminal velocities, *J. Atmos. Sci.*, **53**, 1710–1723, doi:10.1175/1520-0469(1996)053<1710:UOMAAD>2.0.CO;2.
- Mitchell, D. L., and A. J. Heymsfield (2005), Refinements in the treatment of ice particle terminal velocities, highlighting aggregates, *J. Atmos. Sci.*, **62**, 1637–1644, doi:10.1175/JAS3413.1.
- Morrison, H., M. D. Shupe, J. O. Pinto, and J. A. Curry (2005), Possible roles of ice nucleation mode and ice nuclei depletion in the extended lifetime of Arctic mixed-phase clouds, *Geophys. Res. Lett.*, **32**, L18801, doi:10.1029/2005GL023614.
- Morrison, H., J. O. Pinto, J. A. Curry, and G. M. McFarquhar (2008), Sensitivity of modeled Arctic mixed-phase stratocumulus to cloud condensation and ice nuclei over regionally varying surface conditions, *J. Geophys. Res.*, **113**, D05203, doi:10.1029/2007JD008729.
- Morrison, H., et al. (2009), Intercomparison of model simulations of mixed-phase clouds observed during the ARM Mixed-Phase Arctic Cloud Experiment. II: Multi-layered cloud, *Q. J. R. Meteorol. Soc.*, **135**, 1003–1019, doi:10.1002/qj.415.
- Mossop, S. C. (1970), Concentrations of ice crystals in clouds, *Bull. Am. Meteorol. Soc.*, **51**, 474–479, doi:10.1175/1520-0477(1970)051<0474:COICIC>2.0.CO;2.
- Mossop, S. C. (1985), The origin and concentration of ice crystals in clouds, *Bull. Am. Meteorol. Soc.*, **66**, 264–273, doi:10.1175/1520-0477(1985)066<0264:TOACOL>2.0.CO;2.
- Persson, P. O. G., C. W. Fairall, E. L. Andreas, P. S. Guest, and D. K. Perovich (2002), Measurements near the Atmospheric Surface Flux Group tower at SHEBA: Near-surface conditions and surface energy budget, *J. Geophys. Res.*, **107**(C10), 8045, doi:10.1029/2000JC000705.
- Pinto, J. O. (1998), Autumnal mixed-phase cloudy boundary layers in the Arctic, *J. Atmos. Sci.*, **55**, 2016–2038, doi:10.1175/1520-0469(1998)055<2016:AMPCBL>2.0.CO;2.
- Prenni, A. J., et al. (2007), Can ice-nucleating aerosols affect Arctic seasonal climate?, *Bull. Am. Meteorol. Soc.*, **88**, 541–550, doi:10.1175/BAMS-88-4-541.
- Prenni, A. J., P. J. DeMott, D. C. Rogers, S. M. Kreidenweis, G. M. McFarquhar, G. Zhang, and M. R. Poellot (2009), Ice nuclei characteristics from M-PACE and their relation to ice formation in clouds, *Tellus, Ser. B*, **61**, 436–448, doi:10.1111/j.1600-0889.2009.00415.x.
- Protat, A., D. Bouniol, E. J. O'Connor, H. K. Baltink, J. Verlinde, and K. Widener (2011), CloudSat as a global radar calibrator, *J. Atmos. Oceanic Technol.*, **28**, 445–452, doi:10.1175/2010JTECHA1443.1.
- Rambukkange, M. P., J. Verlinde, E. W. Eloranta, C. J. Flynn, and E. E. Clothiaux (2011), Using Doppler spectra to separate hydrometeor populations and analyze ice precipitation in multilayered mixed-phase clouds, *Geosci. Remote Sens. Lett. IEEE*, **8**, 108–112, doi:10.1109/LGRS.2010.2052781.
- Rauber, R. M. (1987), Characteristics of cloud ice and precipitation during wintertime storms over the mountains of Northern Colorado, *J. Clim. Appl. Meteorol.*, **26**(4), 488–524, doi:10.1175/1520-0450(1987)026<0488:COCIAP>2.0.CO;2.
- Rogers, D. C., P. J. DeMott, and S. M. Kreidenweis (2001), Airborne measurements of tropospheric ice-nucleating aerosol particles in the Arctic spring, *J. Geophys. Res.*, **106**, 15,053–15,063, doi:10.1029/2000JD900790.
- Rosinski, J., and G. Morgan (1991), Cloud condensation nuclei as a source of ice-forming nuclei in clouds, *J. Aerosol Sci.*, **22**, 123–133, doi:10.1016/0021-8502(91)90022-A.
- Schmitt, C. G., and A. J. Heymsfield (2005), Total surface area estimates for individual ice particles and particle populations, *J. Appl. Meteorol.*, **44**, 467–474, doi:10.1175/JAM2209.1.
- Shupe, M. D., and J. M. Intrieri (2004), Cloud radiative forcing of the Arctic surface: The influence of cloud properties, surface albedo, and solar zenith angle, *J. Clim.*, **17**, 616–628, doi:10.1175/1520-0442(2004)017<0616:CRFOTA>2.0.CO;2.
- Shupe, M. D., S. Y. Matrosov, and T. Uttal (2006), Arctic mixed-phase cloud properties derived from surface-based sensors at SHEBA, *J. Atmos. Sci.*, **63**, 697–711, doi:10.1175/JAS3659.1.
- Shupe, M. D., P. Kollias, P. O. G. Persson, and G. M. McFarquhar (2008a), Vertical motions in Arctic mixed-phase stratiform clouds, *J. Atmos. Sci.*, **65**, 1304–1322, doi:10.1175/2007JAS2479.1.
- Shupe, M. D., P. Kollias, M. Poellot, and E. Eloranta (2008b), On deriving vertical air motions from cloud radar Doppler spectra, *J. Atmos. Oceanic Technol.*, **25**, 547–557, doi:10.1175/2007JTECHA1007.1.
- Solomon, A., H. Morrison, O. Persson, M. D. Shupe, and J.-W. Bao (2009), Investigation of microphysical parameterizations of snow and ice in Arctic clouds during M-PACE through model-observation comparisons, *Mon. Weather Rev.*, **137**, 3110–3128, doi:10.1175/2009MWR2688.1.
- Stevens, B., W. R. Cotton, G. Feingold, and C.-H. Moeng (1998), Large-eddy simulations of strongly precipitating, shallow, stratocumulus-topped boundary layers, *J. Atmos. Sci.*, **55**, 3616–3638, doi:10.1175/1520-0469(1998)055<3616:LESOSP>2.0.CO;2.
- Stevens, B., et al. (2005), Evaluation of large-eddy simulations via observations of nocturnal marine stratocumulus, *Mon. Weather Rev.*, **133**, 1443–1462, doi:10.1175/MWR2930.1.
- Stevens, D. E., A. S. Ackerman, and C. S. Bretherton (2002), Effects of domain size and numerical resolution on the simulation of shallow cumulus convection, *J. Atmos. Sci.*, **59**(23), 3285–3301, doi:10.1175/1520-0469(2002)059<3285:EODSAN>2.0.CO;2.
- Toon, O. B., C. P. McKay, T. P. Ackerman, and K. Santhanam (1989), Rapid calculation of radiative heating rates and photodissociation rates in inhomogeneous multiple scattering atmospheres, *J. Geophys. Res.*, **94**(D13), 16,287–16,301, doi:10.1029/JD094iD13p16287.
- van Diedenhoven, B., A. M. Fridlind, A. S. Ackerman, E. W. Eloranta, and G. M. McFarquhar (2009), An evaluation of ice formation in large-eddy simulations of supercooled Arctic stratocumulus using ground-based lidar and cloud radar, *J. Geophys. Res.*, **114**, D10203, doi:10.1029/2008JD011198.
- Verlinde, J., et al. (2007), The Mixed-Phase Arctic Cloud Experiment, *Bull. Am. Meteorol. Soc.*, **88**, 205–221, doi:10.1175/BAMS-88-2-205.
- Westbrook, C. D., R. J. Hogan, and A. J. Illingworth (2008), The capacitance of pristine ice crystals and aggregate snowflakes, *J. Atmos. Sci.*, **65**, 206–219, doi:10.1175/2007JAS2315.1.
- Zhang, M. H., and J. L. Lin (1997), Constrained variational analysis of sounding data based on column-integrated budgets of mass, heat, moisture, and momentum: Approach and application to ARM measurements, *J. Atmos. Sci.*, **54**, 1503–1524, doi:10.1175/1520-0469(1997)054<1503:CVAOSD>2.0.CO;2.
- Zhang, M. H., J. L. Lin, R. T. Cederwall, J. J. Yio, and S. C. Xie (2001), Objective analysis of ARM IOP Data: Method and sensitivity, *Mon.*

- Weather Rev.*, 129, 295–311, doi:10.1175/1520-0493(2001)129<0295:OAOAID>2.0.CO;2.
- Zuidema, P., et al. (2005), An Arctic springtime mixed-phase cloudy boundary layer observed during SHEBA, *J. Atmos. Sci.*, 62, 160–176, doi:10.1175/JAS-3368.1.
- 
- A. S. Ackerman and A. M. Fridlind, NASA Goddard Institute for Space Studies, 2880 Broadway, New York, NY 10025, USA.
- A. Avramov, Department of Earth, Atmospheric, and Planetary Sciences, 77 Massachusetts Ave., Rm. 54-1415, Massachusetts Institute of Technology, Cambridge, MA 02139-4307, USA. (lz4ax@mit.edu)
- K. Aydin and G. Botta, Department of Electrical Engineering, Pennsylvania State University, 301 Electrical Engineering East, University Park, PA 16802, USA.
- S. D. Brooks and A. Glen, Department of Atmospheric Sciences, Texas A&M University, 3150 TAMU, College Station, TX 77843-3150, USA.
- R. Jackson and G. M. McFarquhar, Department of Atmospheric Sciences, University of Illinois at Urbana-Champaign, 105 S. Gregory Street, Urbana, IL 61801-3070, USA.
- A. V. Korolev and J. W. Strapp, Science and Technology Branch, Environment Canada, 4905 Dufferin St., Toronto, ON M3H 5T4, Canada.
- B. van Dierenhoven, Center for Climate Systems Research, Columbia University, 2880 Broadway, New York, NY 10025, USA.
- J. Verlinde, Department of Meteorology, Pennsylvania State University, 503 Walker Bldg., University Park, PA 16802, USA.
- M. Wolde, Flight Research Laboratory, National Research Council, Ottawa, ON K1A 0R6, Canada.